

Polar phasing and cross-equatorial heat transfer following a simulated abrupt NH warming of a glacial climate

Article

Accepted Version

Moreno-Chamarro, E., Ferreira, D. ORCID:
<https://orcid.org/0000-0003-3243-9774> and Marshall, J. (2020)
Polar phasing and cross-equatorial heat transfer following a
simulated abrupt NH warming of a glacial climate.
Paleoceanography and paleoclimatology, 35 (7).
e2019PA003810. ISSN 2572-4525 doi:
<https://doi.org/10.1029/2019PA003810> Available at
<https://centaur.reading.ac.uk/95200/>

It is advisable to refer to the publisher's version if you intend to cite from the work. See [Guidance on citing](#).

To link to this article DOI: <http://dx.doi.org/10.1029/2019PA003810>

Publisher: Wiley

All outputs in CentAUR are protected by Intellectual Property Rights law, including copyright law. Copyright and IPR is retained by the creators or other copyright holders. Terms and conditions for use of this material are defined in the [End User Agreement](#).

www.reading.ac.uk/centaur

CentAUR

Central Archive at the University of Reading

Reading's research outputs online

Polar phasing and cross-equatorial heat transfer following a simulated abrupt NH warming of a glacial climate

E. Moreno-Chamarro ^{1,2,*}, D. Ferreira ³, and J. Marshall ¹

1. Department of Earth, Atmospheric, and Planetary Sciences. Massachusetts Institute of Technology, Cambridge, MA, USA.

2. Present address: Barcelona Supercomputing Center (BSC), Barcelona, Spain.

3. Department of Meteorology, University of Reading, Reading, UK

* Corresponding author: eduardo.moreno@bsc.es

Abstract

A ~152–220 year lag between abrupt Greenland warming and maximum Antarctic warming characterizes past glacial Dansgaard–Oeschger events. In a modeling study, we investigate how the cross-equatorial oceanic heat transport (COHT) might drive this phasing during an abrupt Northern Hemisphere (NH) warming. We use the MITgcm in an idealized continental configuration with two ocean basins, one wider, one narrower, under glacial-like conditions with sea ice reaching mid-latitudes. An exaggerated eccentricity-related solar radiation anomaly is imposed over 100 years to trigger an abrupt NH warming and sea-ice melting. The Hadley circulation shifts northward in response, weakening the NH trade winds, subtropical cells, and COHT in both ocean basins. This induces heat convergence in the Southern Hemisphere (SH) ocean subsurface, from where upward heat release melts sea ice and warms SH high-latitudes. Although the small-basin meridional overturning circulation also weakens, driven by NH ice melting, it contributes at most one-third to the total COHT anomaly, hence playing a subsidiary role in the SH and NH initial warming. Switching off the forcing cools the NH; yet heat release continues from the SH ocean subsurface via isopycnal advection-diffusion and vertical mixing, driving further sea ice melting and high-latitude warming for ~50–70 more years. A phasing in polar temperatures resembling reconstructions thus emerges, linked to changes in the subtropical cells' COHT, and SH ocean heat storage and surface fluxes. Our results highlight the potential role of the atmosphere circulation and wind-driven global ocean circulation in the NH–SH phasing seen in DO events.

1. Introduction

The Dansgaard–Oeschger (DO) events during the last glaciation were characterized by abrupt transitions between stadial (colder) and interstadial (warmer) conditions in Greenland temperatures. The latest estimates suggest that Antarctic temperatures peaked ~152–220 years later than the onset of the abrupt Greenland warming (Fig. 1) [WAIS Divide Project Members, 2015; Svensson et al., 2020]. A common theory to explain the phasing between polar temperatures involves the seesaw mechanism, related to changes in the Atlantic meridional overturning circulation (AMOC) and its associated cross-equatorial heat transport [e.g., Broecker, 1998; Stocker and Johnsen, 2003; Knutti et al., 2004; Vettoretti and Peltier, 2015; Lynch-Stieglitz, 2017; Pedro et al., 2018]. During a stadial–interstadial transition, for example, an abrupt Greenland warming is imagined to be driven by a strengthening of the AMOC's northward cross-equatorial oceanic heat transport (COHT) at the expense of cooling Antarctica, and vice versa. The linkage between Northern and Southern polar temperatures has been studied in a variety of modelling studies (see below); however, they show a polar phasing that conflicts not only amongst themselves, but with the latest reconstructions of phasing between Greenland and Antarctic changes. The study of polar phasing is further complicated by the fact that the exact mechanism underlying DO variability remains elusive and a variety of theories are still debated in the literature. Here we describe a sequence of coupled processes that link Northern and Southern temperature changes during and after an abrupt Northern Hemisphere (NH) warming, accounting for their phasing and which do not invoke AMOC as a primary link.

To trigger an abrupt Greenland warming in models, typically an anomalous freshwater flux (hosing) is imposed in the subpolar North Atlantic to weaken the AMOC, which then rapidly increases when the hosing is removed [e.g., Stocker and Johnsen, 2003; Schmittner et al., 2003, Knutti et al., 2004; Menviel et al., 2014; Pedro et al., 2018]. This has a clear warming effect in the North, from where the signal propagates south. Schmittner et al. [2003] proposed two mechanisms to explain such propagation using a climate model of intermediate complexity: a first, fast process associated with the propagation of Kelvin waves throughout the Atlantic Ocean in a few decades, and a second, slower process associated with the modulation of the strength of the Antarctic Circumpolar Current. Based on the time scales of these processes and an analysis of the reconstructed Greenland and Antarctic temperatures, Schmittner et al. [2003] suggested a phasing of about 400–500 years between NH and Southern Hemisphere (SH) polar temperatures. Knutti et al. [2004] found that a maximum Greenland warming was followed by a maximum Antarctic cooling and warming after about 200 and 2000 years respectively. This should be contrasted with the reconstructed Antarctic peak warming ~152–220 years after the Greenland peak warming [WAIS Divide Project Members, 2015; Svensson et al., 2019]. In

Pedro et al. [2018], simulated Antarctic temperatures reach maximum values decades before the onset of the Greenland warming and AMOC strengthening. Other studies using hosing simulations have shown quasi-instantaneous links between Greenland and Antarctic temperatures [e.g., He et al., 2013; Menviel et al., 2014]. Hosing simulations thus show a wide range of polar phasing (from in-phase changes to millennial-scale ones) which are not fully consistent with the latest reconstructions.

Some studies have simulated an abrupt Greenland warming driven by rapid AMOC strengthening through a steady increase in either the height of the Laurentide ice-sheet [Zhang et al., 2014] or atmospheric CO₂ concentration [Banderas et al., 2015; Zhang et al., 2017]. DO-like warming events can also spontaneously arise as a result of non-linear, salt-driven AMOC oscillations in simulations of the last glacial maximum using relatively low values of the ocean vertical mixing [Peltier and Vettoretti, 2014; Vettoretti and Peltier, 2015]. Similarly, abrupt transitions in the intensity and structure of the global overturning circulation emerge in a dynamical box model of the ocean, as a result of nonlinearities in the surface buoyancy distribution in the Southern Ocean and oceanic vertical diffusivity profile [Hines et al., 2019]. In contrast to AMOC-driven warming events, the collapse and re-growth of North Atlantic and Nordic Seas sea ice and ice shelves might drive the DO's initial abrupt warming and later gradual cooling respectively [e.g., Li et al., 2005, 2010; Dokken et al., 2013; Petersen et al., 2013; Sadatzki et al., 2019]. Whenever it is discussed, however, simulated Greenland and Antarctic temperature changes appear to be in phase in these studies [Peltier and Vettoretti, 2014; Zhang et al., 2014; Vettoretti and Peltier, 2015; Banderas et al., 2015; Zhang et al., 2017] and are therefore not in accord with the latest paleo-evidence.

As we have seen, many previous studies have explored linkages between Greenland and Antarctic temperatures by triggering abrupt AMOC changes using freshwater perturbations. In contrast, here we investigate polar phasing and the role of the interhemispheric heat transfer during an abrupt NH warming using a different approach, without making any prior assumptions about the state or role of the AMOC. We trigger an abrupt NH warming through a seasonal redistribution of incoming solar radiation over a year but no net change in its annual mean. We do not seek to reproduce a full DO event, nor support or reject any of the theories about its triggering mechanisms. Rather, our experimental setup is designed to explore the dynamics of global climate adjustment associated with an abrupt NH warming and how the warming signal propagates to the SH. We also compare our model results with those reconstructed during DO events to assess model–proxy consistency.

2. Model description and experimental setup

We use the Massachusetts Institute of Technology general circulation model (MITgcm) in a coupled atmosphere–ocean–sea ice setup [Marshall et al., 1997a; 1997b]. The model exploits an isomorphism between the ocean and atmosphere dynamics to generate an atmospheric GCM and an oceanic GCM from the same dynamical core [Adcroft et al., 2004; Marshall et al., 2004]. Both the atmospheric and oceanic models use the same cubed-sphere grid at the relatively low spatial resolution C24 (i.e., 24 x 24 grid points per face, with a resolution of 3.75° at the Equator). The grid avoids problems associated with converging meridians at the poles and thus ensures that polar dynamics are treated with as much fidelity as elsewhere. The atmospheric physics is of intermediate complexity, based on the simplified parametrizations in the SPEEDY scheme [Molteni, 2003] which is embedded in a 5-level dynamical model. The atmospheric model employs a four-band radiation scheme, a parametrization of moist convection, diagnostic clouds, and a boundary layer scheme. The ocean model has 15 vertical levels, with depth levels increasing from 30 m at the surface to 400 m at depth, with a flat bottom at 3 km depth. The sea ice model uses the two-and-a-half-layer thermodynamic model described in Winton [2000]. Prognostic variables are ice fraction, snow and ice thickness, and a two-level enthalpy representation including brine pockets and sea ice salinity, using an energy-conserving formulation. There are no sea ice dynamics. The land model is a simple two-layer scheme with prognostic temperature, liquid groundwater, and snow height. There is no continental ice. The seasonal cycle is represented, but there is no diurnal cycle. Fluxes of momentum, freshwater, heat, salt, and CO₂ are exchanged every hour (the oceanic time step). The present coupled model achieves perfect (i.e., machine accuracy) conservation of freshwater, heat, and salt during extended climate simulations [Campin et al., 2008].

The model is run in a highly idealized continental configuration that comprises two 45°-wide land masses between the North Pole and 35°S that define a narrow, Atlantic-like basin and a wide, Pacific-like basin (hereafter, small and large basins respectively), connected by an unblocked Southern Ocean (Fig. 2a). There is no Antarctica-like continent at the South Pole. Despite the idealized configuration, the model represents complex interactions regulating the Earth’s climate system. This includes, for example, a two-cell overturning circulation in the global ocean composed of a lower cell associated with bottom water formation in the Southern Hemisphere and an upper AMOC-like cell associated with deep convection in the small basin (Supp. Fig. 1) [Ferreira et al., 2018]. This configuration supports two stable equilibrium climate states for the same external forcing parameters, one cold and one warm [Ferreira et al., 2018]. The cold state presents features resembling the last glacial maximum, with expanded sea ice and land snow cover down to mid-latitudes (~45°) in both hemispheres, an intensified

bottom overturning cell and a weakened overturning circulation in the small basin (Supp. Fig. 1), and a lower CO₂ concentration of about 157 ppm (compared to 268 ppm in the warm state). A detailed description of the differences between these two climate states and how the two states were reached is presented in Ferreira et al. [2018]. Transitions between the warm and cold states triggered by volcanoes are described in Mukund et al. [2019]. We use the cold, glacial-like state as our reference state from which we trigger abrupt NH warming events.

An abrupt NH warming is triggered by an anomaly in the daily-mean top-of-the-atmosphere total solar irradiance (TSI) resulting from setting the eccentricity as 0.1 (compared to the present-day value of ~ 0.017 ; Huybers, 2006). Such a value is unrealistically large because it roughly doubles the maximum value of the Earth's eccentricity over the past 5 Myr [Huybers, 2006]; however, this allows us to trigger a strong climatic response and, in so doing, increase the signal-to-noise ratio. The obliquity is set at the present-day value, equal to 23.5° , and the precession angle is set as 90° (that is, the boreal summer solstice occurs at perihelion). The resulting TSI anomaly exhibits strong seasonal variations in both hemispheres of up to $\sim 100 \text{ W/m}^2$ in mid-latitudes but no change in its annual global average, compared to that of the reference state (Fig. 2b).

In a first experiment, a TSI anomaly is imposed as a step function over 100 model years (Fig. 3a), a long enough period to ensure it excites a dynamical response in the ocean. In a second experiment, the TSI anomaly is imposed over 200 model years to test whether our conclusions depend on the duration of the forcing. In both cases, the model is run on for at least 550 years in total. In a third experiment, the same TSI anomaly is imposed over 100 years, but only in the NH (i.e., anomaly values are set to zero in the SH). To avoid a sharp anomaly drop at the Equator, we apply a spatial smoothing factor (a *tanh* with half width of a degree at the Equator, $0.5 \times [1 + \tanh(\phi/4)]$, where ϕ is the latitude). This experiment is run for only 350 years, as climate conditions return to the cold state faster than in the other simulations (see below). This experimental setup helps clarify the mechanisms behind the interhemispheric heat transfer during an abrupt NH warming. Since the dynamical responses are similar in the global and NH-only experiments, we focus on the simulation with global forcing.

3. Results of transition experiments induced by northern hemispheric warming

The imposed TSI anomaly (Fig. 3a), and especially the summer increase, forces a large, rapid sea surface temperature (SST) warming, sea ice melting and northward retreat in both NH ocean basins during the first 100 years (Figs. 3c,d, 4, and 5a,b). Sea ice melting results in the ocean absorbing more solar radiation, leading to further upper-ocean warming and sea ice melting. The ocean warming

extends into the lower atmosphere and poleward above the sea ice cap (Figs. 3b, 4). This strengthens the meridional (Fig. 4) and vertical (not shown) temperature gradient in NH mid-latitudes, which intensifies surface westerlies and shifts them further northward (Fig. 5a,b). Such a change in zonal winds, with anomalous westerlies/easterlies to the north/south of the sea ice edge, drives an anomalous surface ocean circulation of convergence and downwelling in mid-latitudes (Fig. 5a,b). This change drives further upper-ocean warming (Fig. 6a), strengthening ocean heat uptake in the NH over the first 100 years (Fig. 7 and Supp. Fig. 2).

About half of the anomaly in the NH surface ocean heat uptake is nonetheless compensated by a southward COHT anomaly in the first 100 years (Fig. 7, top), to which both ocean basins contribute in almost equal parts (Fig. 3e). This anomaly is mainly driven by a weakening of the NH subtropical cells (STCs) in both ocean basins and, to a lesser extent, by a weakening of the meridional overturning circulation in the small basin (SMOC; Figs. 3f). The STC weakening is a consequence of a decrease in the NH zonal trade winds (Fig. 5a,b) in response to a northward shift of the Hadley circulation (Supp. Fig. 3) and Intertropical Convergence Zone (ITCZ; Green and Marshall, 2017; McGee et al., 2018). This shift also drives a southward anomaly in the cross-equatorial atmospheric heat transport (CAHT; Fig. 2) which partially compensates for the interhemispheric atmospheric heating imbalance [e.g., Donohoe et al., 2013; Marshall et al., 2014; Schneider et al., 2014]. Although, in our model, the CAHT anomaly develops on shorter time scales than that in the COHT (Fig. 3e), its magnitude is only half of that in the ocean (about -0.1 PW and -0.2 PW respectively; Fig. 3e). The northward Hadley cell shift is nonetheless key to the weakening of the NH STCs which drives most of the southward COHT anomaly (Fig. 3)—see Green and Marshall [2017].

The SMOC also weakens during the first 100 years with the forcing active. The NH upper-ocean warming (Figs. 4, 5, and 6) and freshening (Supp. Fig. 4) due to the rapid ice melting, strongly decrease ocean deep convection in the small basin (not shown). Thus, the SMOC does not drive the rapid NH warming in the model. We approximate the SMOC's COHT by assuming that the STC's COHT is proportional to the ocean basin width [Forget and Ferreira, 2019] and, therefore, that the small basin STC contribution is half that of the large basin (Fig. 3e). Interestingly, the SMOC's COHT inferred this way (Fig. 3e,f), consistent with a simple scaling for the SMOC COHT given by $\rho \Delta T W$ (where ΔT is the temperature difference between the upper and lower limbs of the SMOC and is 10 °C approximately). This suggests that the SMOC's COHT contributes between one quarter to one third of the total southward COHT anomaly in the first 100 years (Fig. 3e), with the remaining anomaly driven by the STCs. Additionally, while the STC responds quasi-instantaneously to

the NH trade wind changes, the SMOC adjustment develops on longer (multi-decadal) time scales. The weakening of both NH STCs is therefore key to explaining the COHT changes in the first 100 years and, by extension, the warming of the SH ocean (see below).

In the first 100 years, both hemispheres show a similar warming rate in the ocean (Fig. 7, bottom), even though the SH SST warming is weaker than in the NH (Figs. 3c). Unlike in the NH case, changes in the air–sea heat flux have a negligible contribution to the total SH ocean warming. The latter is almost completely driven by the southward COHT anomaly and the associated heat convergence in the ocean subsurface. This is further evidenced by the fact that the SH warming between 40°S and the Equator begins in the subsurface (with a peak around ~150 m) and steadily propagates to the surface (Fig. 6, bottom). The SH SST warming, however, is initially partly offset by the effect of the imposed forcing: due to its seasonality, TSI anomalies are negative during the austral summer with respect to cold state values. This induces a SST cooling and sea ice expansion in the first few years (Figs. 2, 4, and 6), a time when the warming propagating from the subsurface is still developing. Eventually, both SH mid-latitude SST and mid- and high latitude SAT over the ice cap begin to warm progressively, at a slower and weaker rate than in the NH (Fig. 3b,c). The mechanisms driving the changes in polar temperature and in the CAHT and COHT are summarized in Fig. 8.

Once the forcing is switched off, the NH ocean begins to release heat stored in the upper 1000 m (Fig. 7, top). However, the amount of heat in the NH ocean does not decrease until about year 300, as the surface heat release is compensated by an anomalous northward COHT in both basins (Figs. 3e and 7). Since the STC anomalies rapidly vanish in a couple of decades (Fig. 3f), following the changes in the Hadley circulation (Supp. Fig. 3) and trade winds (Fig. 5c,d), the STC contribution to the anomalous northward OHT is therefore likely due to the heat stored in the SH ocean. In addition, the SMOC steadily strengthens after a minimum value around year 100, and becomes anomalously stronger than its cold-state climatology after ~200 years, thus contributing to the northward COHT anomaly (Fig. 3e,f). The SMOC strengthening is caused by an increase in upper-ocean salinity (Supp. Fig. 4) and a northward shift and intensification of deep convection in the small basin over the first 100 years (not shown). Such a northward COHT anomaly helps sustain warm conditions and reduced sea ice extent in mid- and high latitudes in the small basin for a longer period than in the large basin (Fig. 4). Thus, although the SMOC is not the main driver of the initial, rapid NH warming, its overshoot after the forcing is shut off plays a role in the slower return to normal conditions in the small basin.

In the SH, the SST and SAT warming and the sea ice melting continue after the forcing is switched off, reaching maximum anomalies between ~125–175 years (Figs. 3b,c and 4). These changes are initially triggered by the release of heat stored in the ocean subsurface (as suggested by Fig. 6) most likely through a combination of isopycnal advection-diffusion and vertical mixing (not shown). As mid-latitude SSTs warm, they contribute to further sea ice melting, whose edge retreats southward (Fig. 4). Sea ice melting, in turn, amplifies the SST warming by increasing the local ocean surface heat uptake (Supp. Fig. 2), as happens in the NH in the first 100 years with the forcing on. This mechanism contributes to extending the SH mid-latitude SST and high-latitude SAT warming with respect to the NH and thus sets the phasing between the NH and SH high-latitude temperatures (Fig. 4). The time scale of the phasing is determined by the release of heat from the subsurface in mid-latitudes (Fig. 6). The surface warming mechanism acts at the ice edge locally and impacts SAT south of 35°S. Nonetheless, with the forcing off, the SH ocean as a whole shifts from gaining heat to losing it, largely through advection across the Equator into the NH (Fig. 7). This is summarized in Supp. Fig. 5.

The simulation with a 200-year forcing shows similar results to those described above, with SH warming continuing 50 more years or so compared to the NH warming after the forcing is switched off (Supp. Fig. 6). As expected from the larger amount of heat added, this simulation exhibits a longer return period than the 100-year long forcing experiment.

The experiment with forcing only in the NH shows similar results to those with a global forcing, including the phasing between the NH and SH warming, but with anomalies of smaller magnitude (Supp. Figs 7, 8, and 9). The SH ocean exhibits net heat release in the first 100 years in this experiment, in contrast with the near-zero anomalies in the experiment with global forcing. This reinforces our interpretation that heat stored in the SH is partially released at the SH surface and later on returned to the NH, after the forcing has been switched off. This also suggests that the seasonality in the forcing in the SH and the related initial cooling described above have no effect on the characteristics of the polar phasing.

4. Discussion

The simulated phasing between the maximum warming at NH and SH high-latitudes is about 50 years, regardless of the length of the forcing and whether it is imposed only in the NH. The latest reconstructions suggest a similar but somewhat longer north-to-south signal propagation of about 152 ± 37 to 218 ± 92 years on average during a DO abrupt warming (Fig. 1) [WAIS Divide Project Members, 2015; Svensson et al., 2020]. Considering the simplicity of our model setup—two flat,

triangular continents, no ice sheet or land processes, no Antarctica, and relatively low spatial ocean and atmosphere model resolutions—the similarity of the time scale between model and observation is notable. This suggests that the adjustment mechanisms described in our simulations are likely to have also operated during past glacial DO events. Such mechanisms highlight the role of changes in global tropical ocean circulation induced by trade wind shifts in accumulating heat in the SH ocean, and not changes in AMOC. Heat convergence in the SH and its eventual release to the mid-latitude and polar atmosphere are key to setting the phasing between the NH and SH warming, once the forcing is switched off.

Our conclusion is reinforced by the fact that, despite the highly idealized experimental setup, the model reproduces some key climate changes reconstructed during DO events. For example, the simulated northward ITCZ shift is consistent with precipitation proxies suggesting an increase in precipitation in NH regions, such as the Cariaco Basin [Deplazes et al., 2013], the Arabian Sea [Deplazes et al., 2013], and Eastern China [Wang et al., 2001], and a decrease in precipitation in SH locations, such as Brazil [Wang et al., 2007], Peru [Kanner et al., 2013], and Ecuador [Mosbloch et al., 2012]. Besides changes in precipitation, the simulated quasi-instantaneous response in the wind field to the imposed forcing is consistent with reconstructions suggesting synchronous changes between Greenland temperatures and the Southern Ocean wind pattern during DO events [Markle et al. 2016]. In addition, changes in oceanographic conditions at mid- and high latitudes in the small basin between the cold state and year 100 with the forcing active (Supp. Fig. 10) are in accord with reconstructed changes in the Nordic Seas [Dokken et al., 2013]: cold stadials present mostly sea-ice covered conditions and a strong halocline at the surface with warm waters underneath, whereas warm interstadials present nearly ice-free surface conditions and warm waters reaching the ocean surface. The dominant role of sea ice in setting temperature changes at high latitudes in the model is also consistent with reconstructed sea ice changes in the Nordic Seas [Sadatzki et al., 2019]. The model further simulates a very small increase in the atmospheric CO₂ concentration (about 2 ppm by year 100; not shown) due to the NH warming which is consistent with the insignificant change reconstructed in DO events [Ahn and Brook, 2014]. However, it is unclear how the simulated SMOC weakening and later strengthening can be reconciled with the reconstructed increase in the flow speed of the North Atlantic Deep Water in the subpolar North Atlantic [Kissel et al., 2008] or with changes in Pa/Th ratio [Henry et al., 2016], which suggest a reinforced AMOC during interstadial periods; these proxies, nevertheless, are subject to relatively low dating precision and temporal resolution which might hamper their interpretation.

The change in orbital forcing employed in our study to drive abrupt NH warming might not be optimal to explain actual DO variability. The forcing is chosen to be large to increase signal-to-noise ratio, as described in Section 2, and we therefore cannot rule out that the model response might be exaggerated with respect to the reconstructed climate changes. Furthermore, the time scale of the orbital forcing does not match that of full DO cycles [Dansgaard et al., 1993]. That said, here we do not attempt to disentangle the triggering mechanism of DO events. The prescribed forcing is used to trigger a response of the climate system to a NH warming and decipher the resulting dynamical and response timescales. Our experimental setup and chosen forcing is fundamentally different from previous investigations, which have mostly relied on a freshwater flux anomaly to modulate the AMOC strength [e.g., Stocker and Johnson, 2003; Knutti et al., 2004; Pedro et al., 2018; among others]. Although some works have considered external forcing such as growing ice sheets [Zhang et al., 2014] or a varying CO₂ concentration [Banderas et al., 2015; Zhang et al., 2017], their goal was to trigger an abrupt AMOC strengthening to warm the NH. In our simulations, instead, the climate is forced to respond to an abrupt NH warming, without assuming it needs to be driven by the AMOC. We find that surface temperatures mainly respond to sea ice changes and that a polar phasing emerges in the model set by the evolution of the COHT, and SH ocean heat storage and surface fluxes. In summary, even though an abrupt AMOC strengthening is nowadays the most favored theory to explain the Greenland warming during DO events [e.g., Lynch-Stieglitz, 2017], we show that our simulations can reproduce other climate changes associated with DO variability without the need of an AMOC strengthening.

5. Conclusions

We have investigated the mechanism underlying the phasing between NH and SH high-latitude temperatures during an abrupt NH warming. We use a coupled ocean–atmosphere–sea ice based on the MITgcm in an idealized configuration with two land masses which extend from the North Pole down to 35°S and separate a narrow, Atlantic-like ocean basin and a wide, Pacific-like one. An abrupt NH warming is forced by an increase in the Earth’s eccentricity and a shift to vernal equinox at perihelion, which modifies the TSI distribution throughout the year but not its annual, global mean. This experimental setup does not attempt to simulate an entire DO event but rather to investigate the processes that might have driven the reconstructed ~152–220 year polar phasing [WAIS Divide Project Members, 2015; Svensson et al., 2019]. Three simulations are performed, with the forcing

applied over 100 years, 200 years, and over 100 years but only in the NH. As summarized in Fig. 8, our model results indicate that:

1. With the forcing on:

1.1 NH mid- and high-latitudes experience abrupt SAT and SST warming and sea ice melting. The warming drives a quasi-instantaneous ITCZ and Hadley circulation northward shift. This, in turn, weakens the NH trade winds and, as a result, the STCs in both ocean basins. On longer (decadal) time scales, the sea ice melting and upper-ocean freshening also drive a SMOC weakening.

1.2. Roughly half of the NH ocean warming is compensated by a southward COHT anomaly. The STC weakening contributes the most, explaining between two-thirds and three-quarters of the CHOT anomaly, while SMOC weakening contributes the remainder. The northward Hadley circulation shift induces a southward CAHT anomaly which is only half the magnitude of the COHT anomaly.

1.3. As a result of the southward COHT anomaly, heat accumulates in the SH ocean subsurface in mid-latitudes on the same timescales as the NH abrupt warming. From the subsurface, heat propagates upward, warming the mixed layer and melting sea ice, eventually warming the lower atmosphere over the SH ice cap at high-latitudes; this mechanism, however, occurs at a slower rate and leads to a dampened SAT warming compared to the NH (Fig. 8).

2. With the forcing off:

2.1 At NH high-latitudes, the two ocean basins begin to cool down immediately as sea ice re-grows. The Hadley cell, the ITCZ, and by extension the STCs, also return to their climatological positions in less than 50 years. The SMOC, by contrast, returns to its control value after ~100 years. It then overshoots, inducing a northward COHT anomaly in the small basin which slows down the cooling rate of the small basin compared to the large one.

2.2. In the SH, heat continues to be released from the subsurface, driving further sea ice melting and SST warming at mid-latitude. This sustains the SAT warming trend above the ice cap, extending it for ~50 more years than in the NH. A phasing between NH and SH polar temperatures thus emerges in the model, set by the initial heat accumulation in the SH ocean subsurface and its eventual release and amplification by melting sea ice.

Despite the simplicity of the experimental setup, the model reproduces important features of the reconstructed climate changes during DO events, such as a NH–SH polar phasing, a northward ITCZ

shift, a quasi-instantaneous coupling between the westerlies and the NH warming, and a nearly negligible change in atmospheric CO₂ concentration.

A critical aspect here is that MOC fluctuations, although important for the model phasing, are not the drivers of the abrupt changes. Our simulations also reveal a consistent set of changes in the atmosphere and the wind-driven circulation of the ocean which are essential in propagating the perturbations from the NH to the SH. Our results emphasize the potential critical role of components of the climate system beyond the AMOC, which should receive more attention in studies of the DO events' dynamics.

Acknowledgments:

E.M.-C. And J.M. acknowledge support from NOAA award NA16OAR4310177. Data and code to reproduce the authors' work can be obtained from <https://doi.org/10.7910/DVN/QJ6VS3>

References

Adcroft, A., & Campin, J. M. (2004). Rescaled height coordinates for accurate representation of free-surface flows in ocean circulation models. *Ocean Modelling*, 7(3), 269–284.

Ahn, J., & Brook, E. J. (2014). Siple Dome ice reveals two modes of millennial CO₂ change during the last ice age. *Nature Communications*, 5.

Banderas, R., Alvarez-Solas, J., Robinson, A., & Montoya, M. (2015). An interhemispheric mechanism for glacial abrupt climate change. *Climate Dynamics*, 44(9-10), 2897–2908.

Broecker, W. S. (1998). Paleocean circulation during the last deglaciation: a bipolar seesaw?. *Paleoceanography*, 13(2), 119–121.

Campin, J. M., Marshall, J., & Ferreira, D. (2008). Sea ice–ocean coupling using a rescaled vertical coordinate z. *Ocean Modelling*, 24(1), 1–14.

Dansgaard, W., Johnsen, S. J., Clausen, H. B., Dahl-Jensen, D., Gundestrup, N. S., Hammer, C. U., ... & Bond, G. (1993). Evidence for general instability of past climate from a 250-kyr ice-core record. *Nature*, 364(6434), 218.

Deplazes, G., Lückge, A., Peterson, L. C., Timmermann, A., Hamann, Y., Hughen, K. A., ... & Haug, G. H. (2013). Links between tropical rainfall and North Atlantic climate during the last glacial period. *Nature Geoscience*, 6(3), 213–217.

Dokken, T. M., Nisancioglu, K. H., Li, C., Battisti, D. S., & Kissel, C. (2013). Dansgaard–Oeschger cycles: Interactions between ocean and sea ice intrinsic to the Nordic Seas. *Paleoceanography*, 28(3), 491–502.

Donohoe, A., Marshall, J., Ferreira, D., & Mcgee, D. (2013). The relationship between ITCZ location and cross-equatorial atmospheric heat transport: From the seasonal cycle to the Last Glacial Maximum. *Journal of Climate*, 26(11), 3597–3618.

Forget, G., & Ferreira, D. (2019). Global ocean heat transport dominated by heat export from the tropical Pacific. *Nature Geoscience*, 12(5), 351.

Ferreira, D., Marshall, J., Ito, T., & McGee, D. (2018). Linking Glacial–Interglacial states to multiple equilibria of climate. *Geophysical Research Letters*, 45(17), 9160–9170.

Green, B. and Marshall, J (2017) Coupling of Trade Winds with Ocean Circulation Damps ITCZ Shifts. *Journal of Climate*, 30, 12, 4395–4411

Gupta, M., Marshall, J., & Ferreira, D. (2019). Triggering global climate transitions through volcanic eruptions. *Journal of Climate*, 32(12), 3727–3742.

He, F., Shakun, J. D., Clark, P. U., Carlson, A. E., Liu, Z., Otto-Bliesner, B. L., & Kutzbach, J. E. (2013). Northern Hemisphere forcing of Southern Hemisphere climate during the last deglaciation. *Nature*, 494(7435), 81–85.

Henry, L. G., McManus, J. F., Curry, W. B., Roberts, N. L., Piotrowski, A. M., & Keigwin, L. D. (2016). North Atlantic ocean circulation and abrupt climate change during the last glaciation. *Science*, 353(6298), 470–474.

Hines, S. K., Thompson, A. F., & Adkins, J. F. (2019). The role of the Southern Ocean in abrupt transitions and hysteresis in glacial ocean circulation. *Paleoceanography and Paleoclimatology*, 34(4), 490–510.

Huybers, P. (2006). Early Pleistocene glacial cycles and the integrated summer insolation forcing. *Science*, 313(5786), 508–511.

Kanner, L. C., Burns, S. J., Cheng, H., & Edwards, R. L. (2012). High-latitude forcing of the South American summer monsoon during the last glacial. *Science*, 335(6068), 570–573.

Kissel, C., Laj, C., Piotrowski, A. M., Goldstein, S. L., & Hemming, S. R. (2008). Millennial-scale propagation of Atlantic deep waters to the glacial Southern Ocean. *Paleoceanography*, 23(2).

Knutti, R., Flückiger, J., Stocker, T. F., & Timmermann, A. (2004). Strong hemispheric coupling of glacial climate through freshwater discharge and ocean circulation. *Nature*, 430(7002), 851–856.

Li, C., Battisti, D. S., & Bitz, C. M. (2010). Can North Atlantic sea ice anomalies account for Dansgaard–Oeschger climate signals?. *Journal of Climate*, 23(20), 5457–5475.

Li, C., Battisti, D. S., Schrag, D. P., & Tziperman, E. (2005). Abrupt climate shifts in Greenland due to displacements of the sea ice edge. *Geophysical Research Letters*, 32(19).

Lynch-Stieglitz, J. (2017). The Atlantic meridional overturning circulation and abrupt climate change. *Annual Review of Marine Science*, 9, 83–104.

Markle, B. R., Steig, E. J., Buizert, C., Schoenemann, S. W., Bitz, C. M., Fudge, T. J., ... & Sowers, T. (2016). Global atmospheric teleconnections during Dansgaard–Oeschger events. *Nature Geoscience*, 10(1), 36–40.

Marshall, J., Adcroft, A., Hill, C., Perelman, L., & Heisey, C. (1997a). A finite-volume, incompressible Navier Stokes model for studies of the ocean on parallel computers. *Journal of Geophysical Research: Oceans*, 102(C3), 5753–5766.

Marshall, J., Hill, C., Perelman, L., & Adcroft, A. (1997b). Hydrostatic, quasi-hydrostatic, and nonhydrostatic ocean modeling. *Journal of Geophysical Research: Oceans*, 102(C3), 5733–5752.

Marshall, J., Adcroft, A., Campin, J. M., Hill, C., & White, A. (2004). Atmosphere–ocean modeling exploiting fluid isomorphisms. *Monthly Weather Review*, 132(12), 2882–2894.

Marshall, J., Donohoe, A., Ferreira, D., & McGee, D. (2014). The ocean’s role in setting the mean position of the Inter-Tropical Convergence Zone. *Climate Dynamics*, 42(7–8), 1967–1979.

McGee, D., Moreno-Chamarro, E., Green, B., Marshall, J., Galbraith, E., & Bradtmiller, L. (2018). Hemispherically asymmetric trade wind changes as signatures of past ITCZ shifts. *Quaternary Science Reviews*, 180, 214–228.

Menviel, L., Timmermann, A., Friedrich, T., & England, M. H. (2014). Hindcasting the continuum of Dansgaard–Oeschger variability: mechanisms, patterns and timing. *Climate of the Past*, 10(1), 63–77.

Molteni, F. (2003). Atmospheric simulations using a GCM with simplified physical parametrizations. I: Model climatology and variability in multi-decadal experiments. *Climate Dynamics*, 20(2), 175–191.

Mosblech, N. A., Bush, M. B., Gosling, W. D., Hodell, D., Thomas, L., Van Calsteren, P., ... & Van Woesik, R. (2012). North Atlantic forcing of Amazonian precipitation during the last ice age. *Nature Geoscience*, 5(11), 817–820.

Pedro, J. B., Jochum, M., Buizert, C., He, F., Barker, S., & Rasmussen, S. O. (2018). Beyond the bipolar seesaw: Toward a process understanding of interhemispheric coupling. *Quaternary Science Reviews*, 192, 27–46.

Peltier, W. R., & Vettoretti, G. (2014). Dansgaard–Oeschger oscillations predicted in a comprehensive model of glacial climate: A “kicked” salt oscillator in the Atlantic. *Geophysical Research Letters*, 41(20), 7306–7313.

Petersen, S. V., Schrag, D. P., & Clark, P. U. (2013). A new mechanism for Dansgaard–Oeschger cycles. *Paleoceanography*, 28(1), 24–30.

Sadatzki, H., Dokken, T. M., Berben, S. M., Muschitiello, F., Stein, R., Fahl, K., ... & Jansen, E. (2019). Sea ice variability in the southern Norwegian Sea during glacial Dansgaard-Oeschger climate cycles. *Science Advances*, 5(3), eaau6174.

Schmittner, A., Saenko, O. A., & Weaver, A. J. (2003). Coupling of the hemispheres in observations and simulations of glacial climate change. *Quaternary Science Reviews*, 22(5), 659–671.

Schneider, T., Bischoff, T., & Haug, G. H. (2014). Migrations and dynamics of the intertropical convergence zone. *Nature*, 513(7516), 45–53.

Svensson, A., Dahl-Jensen, D., Steffensen, J. P., Blunier, T., Rasmussen, S. O., Vinther, B. M., Vallelonga, P., Capron, E., Gkinis, V., Cook, E., Kjær, H. A., Muscheler, R., Kipfstuhl, S., Wilhelms, F., Stocker, T. F., Fischer, H., Adolphi, F., Erhardt, T., Sigl, M., Landais, A., Parrenin, F., Buizert, C., McConnell, J. R., Severi, M., Mulvaney, R., & Bigler, M. (in review, 2020). Bipolar volcanic synchronization of abrupt climate change in Greenland and Antarctic ice cores during the last glacial period. *Climate of the Past Discussion*.

Stocker, T. F., & Johnsen, S. J. (2003). A minimum thermodynamic model for the bipolar seesaw. *Paleoceanography*, 18(4).

Vettoretti, G., & Peltier, W. R. (2015). Interhemispheric air temperature phase relationships in the nonlinear Dansgaard–Oeschger oscillation. *Geophysical Research Letters*, 42(4), 1180–1189.

WAIS Divide Project Members. (2015). Precise inter polar phasing of abrupt climate change during the last ice age. *Nature*, 520(7549), 661–665.

Wang, X., Auler, A. S., Edwards, R. L., Cheng, H., Ito, E., Wang, Y., ... & Solheid, M. (2007). Millennial-scale precipitation changes in southern Brazil over the past 90,000 years. *Geophysical Research Letters*, 34(23).

Wang, Y. J., Cheng, H., Edwards, R. L., An, Z. S., Wu, J. Y., Shen, C. C., & Dorale, J. A. (2001). A high-resolution absolute-dated late Pleistocene monsoon record from Hulu Cave, China. *Science*, *294*(5550), 2345–2348.

Winton, M. (2000). A reformulated three-layer sea ice model. *Journal of Atmospheric and Oceanic Technology*, *17*(4), 525–531.

Zhang, X., Knorr, G., Lohmann, G., & Barker, S. (2017). Abrupt North Atlantic circulation changes in response to gradual CO₂ forcing in a glacial climate state. *Nature Geoscience*, *10*(7), 518–523.

Zhang, X., Lohmann, G., Knorr, G., & Purcell, C. (2014). Abrupt glacial climate shifts controlled by ice sheet changes. *Nature*, *512*(7514), 290–294.

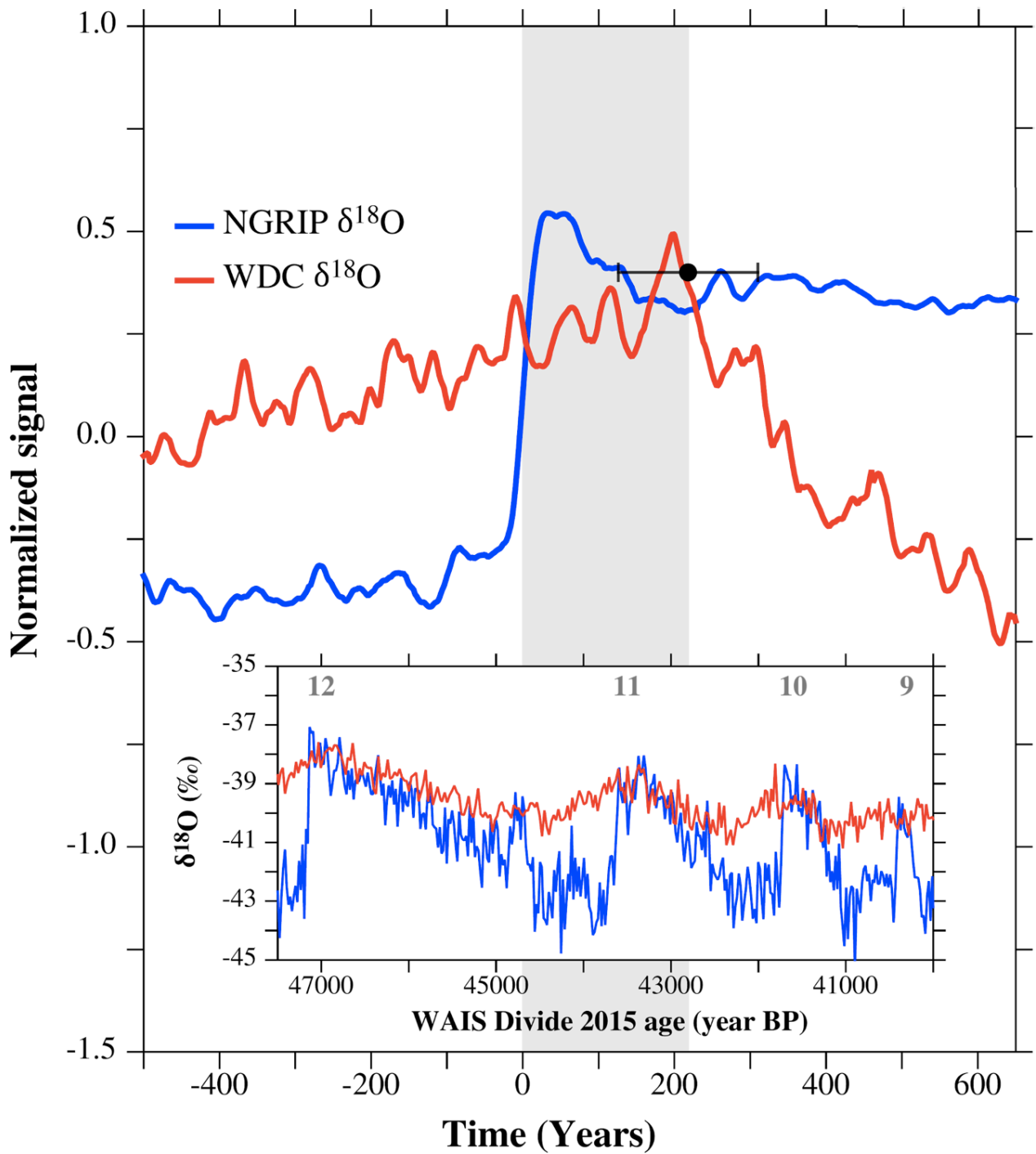


Fig. 1. Composite time series of the $\delta^{18}\text{O}$ (considered a proxy for surface atmosphere temperatures) averaged for DO events 3 to 18 in NGRIP (Greenland; blue line) and WDC (West Antarctica; red line), as in WAIS Divide Project Members [2015]. DO events are averaged with their original amplitudes and normalized afterwards. Shaded vertical gray bars show NH lead time, and the error bar represents the 2σ bounds (i.e., 218 ± 92 years). Inset shows the actual time series of the NGRIP and WDC $\delta^{18}\text{O}$ (in ‰) between 47500 and 40000 years BP, including DO events 9 to 12.

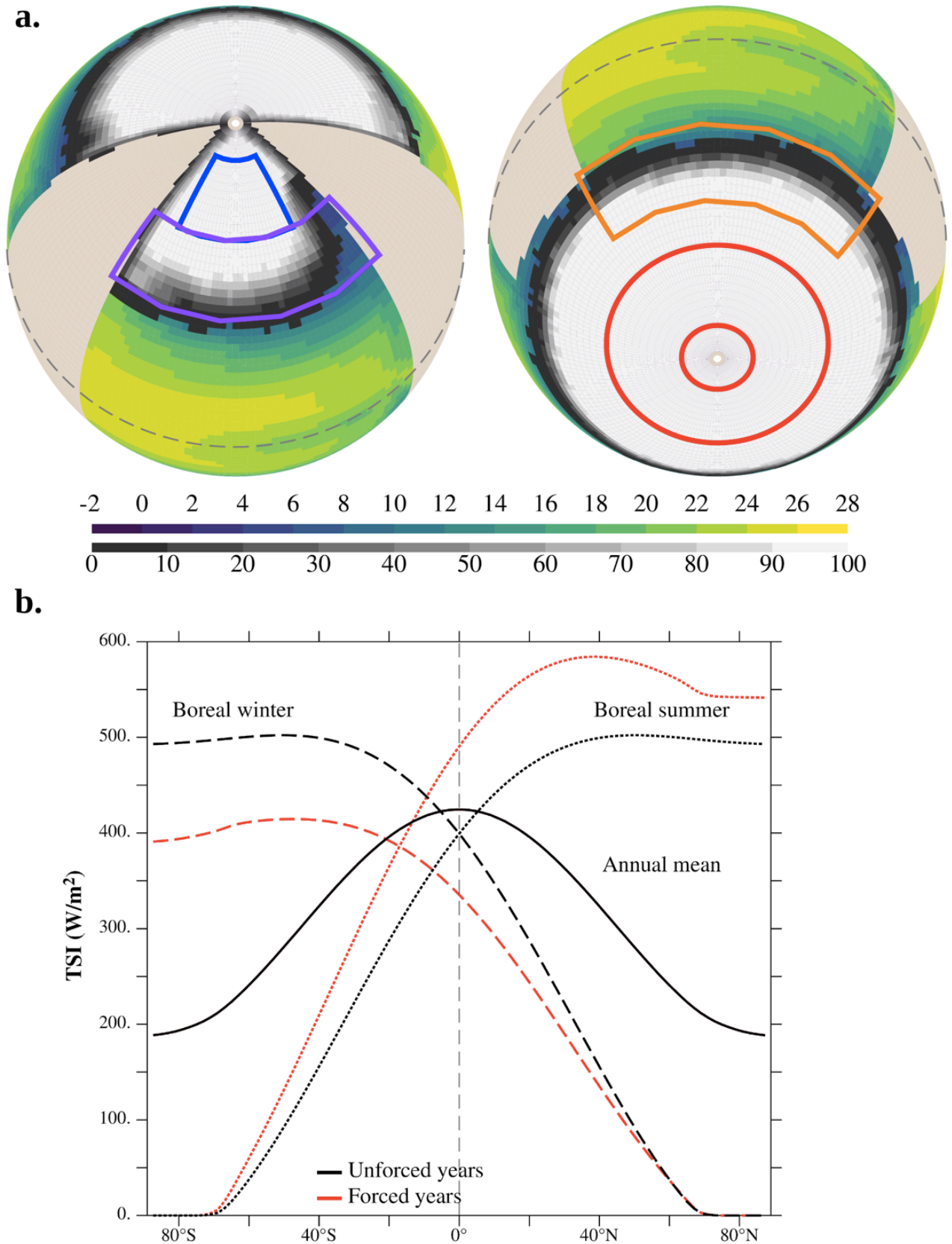


Fig. 2. a) SST (in $^{\circ}\text{C}$; blue–yellow shading) and sea ice concentration (in %; gray shading) in the NH (left) and SH (right) of the cold state. Boxes on both panels outline areas where mean temperatures are calculated in Fig. 3. Equator line is gray and dashed. **b)** Zonally averaged TSI (in W/m^2) in boreal summer (dot line) and winter (dash line), and on annual mean (solid line) in the forced (red) and unforced (black) years.

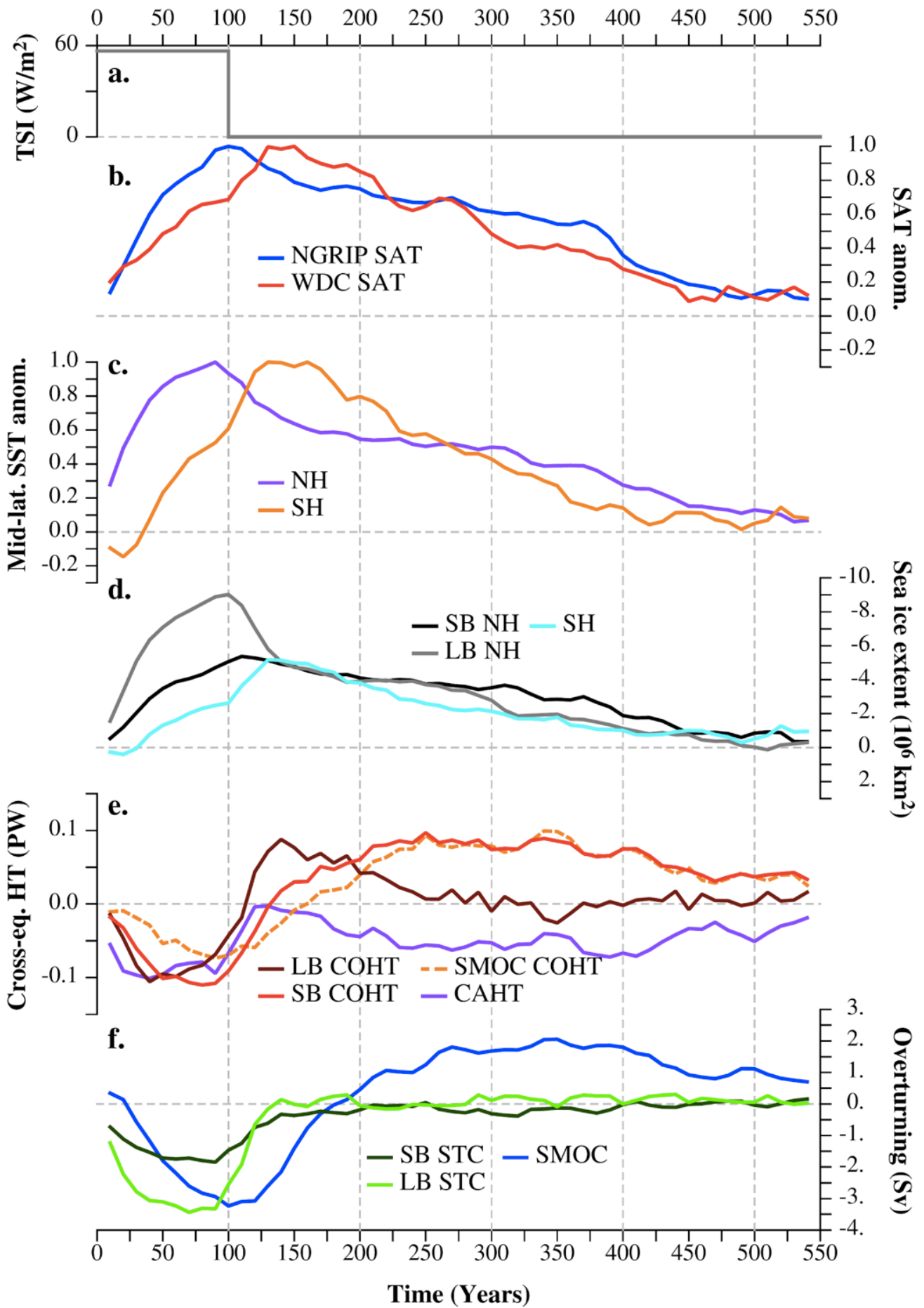


Fig. 3. (Caption next page).

Fig. 3.

a) TSI anomaly (in W/m^2) on average in the NH summer (June–August).

b) SAT anomalies over the NGRIP (blue) and WDC (red) ice core sites in Greenland and West Antarctica respectively (areas shown in blue and red respectively in Fig. 2a). Time series are normalized by their corresponding maximum anomaly value (about 9°C and 3°C respectively).

c) SST anomalies in the small basin at mid-latitude in the NH (40°N – 60°N ; purple) and SH (30°S – 50°S ; purple) both averaged between 95°W and 5°E (areas shown in orange and purple respectively in Fig. 2a). These regions correspond with the latitudes of maximum change in sea ice (see for example Fig. 4). Time series are normalized by their corresponding maximum anomaly value (about 4°C and 1°C respectively).

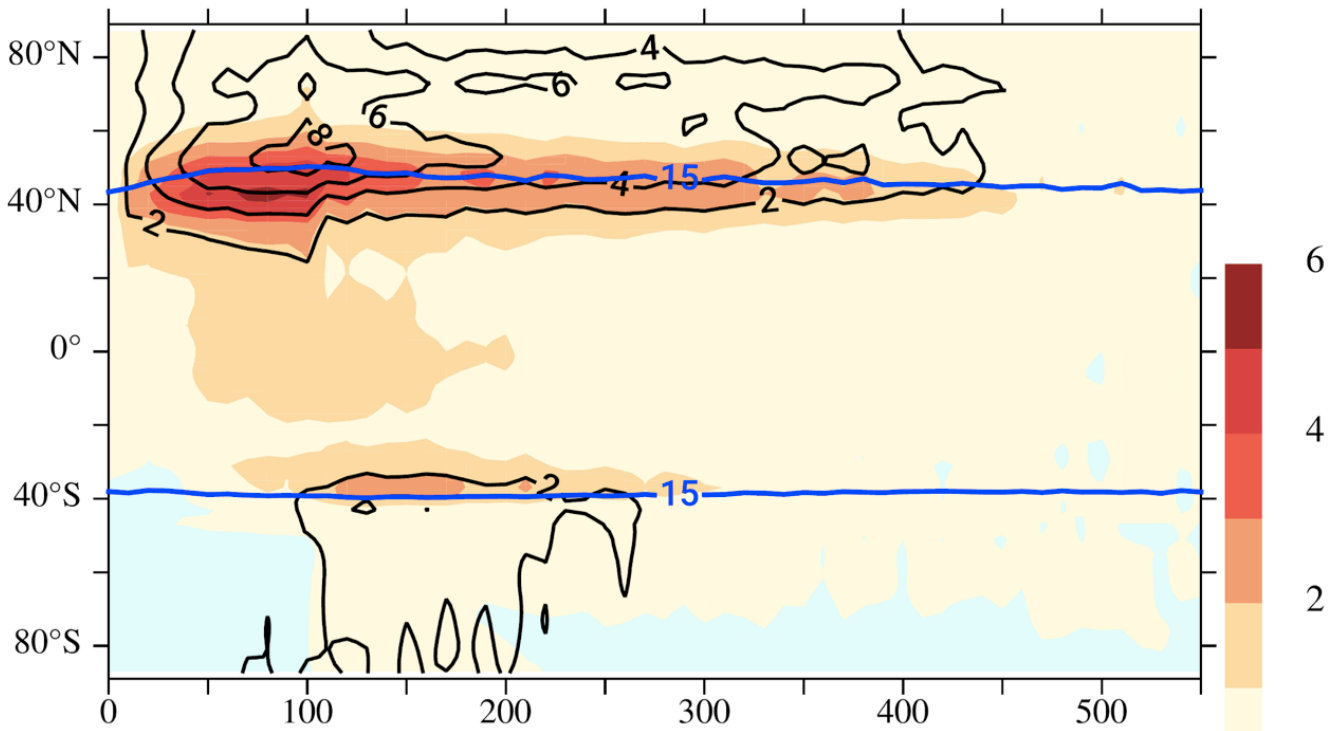
d) Sea ice extent anomalies (in 10^6 km^2) in the NH small and large basin (black and gray respectively) and the whole SH (light blue). Note that the vertical axis is reversed.

e) Anomalies in the cross-equatorial heat transport (in PW) in the large and small ocean basin (LB and SB COHT in dark and light red respectively), and in the atmosphere (CAHT; purple). Also, approximation of the SMOC's CHOT (dashed orange). This is calculated assuming that the STC's COHT is proportional to the width of the ocean basin and, therefore, that SB one is half of the LB one. The SMOC's CHOT is thus equal to SB's total CHOT – $0.5 \cdot \text{LB's total COHT}$.

f) Anomalies (in Sv) in the strength of the SMOC (blue) and STCs in the NH in the small and large basin (dark and light green respectively). The SMOC strength is defined as the average of the overturning streamfunction between 35°N and 45°N at 1000 m, i.e., where the climatological maximum in the cold state is located (Supp. Fig. 1). The STC strengths are defined as the average value of the overturning circulation between 5°N and 20°N between the surface and 250 m depth (Supp. Fig. 1).

(a–f) Anomalies are calculated relative to the cold state. **(b–f)** Decadal time series are smoothed with a 3-point running mean.

a. Small Basin



b. Large Basin

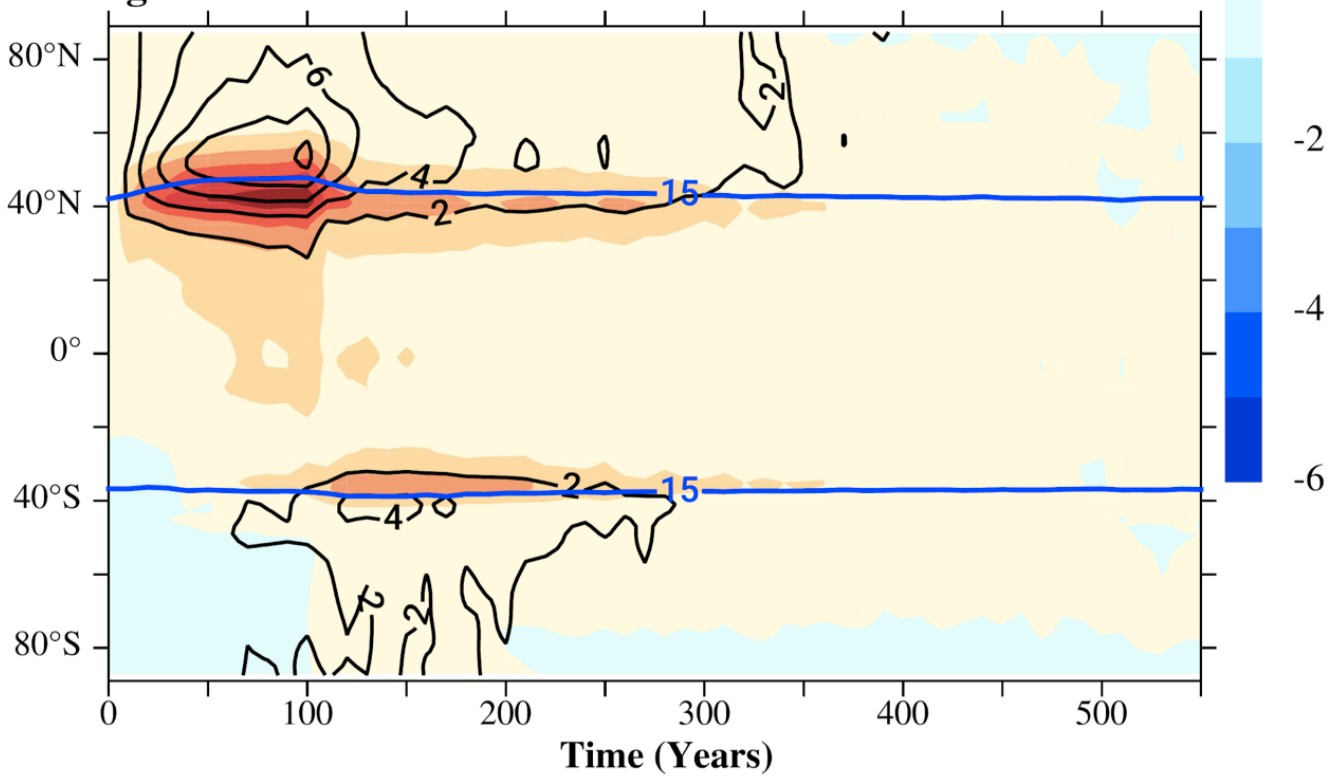


Fig. 4. Anomalies (in °C) in the zonally averaged SST (shading) and SAT (contours) in the (a) small and (b) large basin. Also shown in each basin is the sea ice extent limit, as the 15% sea ice concentration (blue contours).

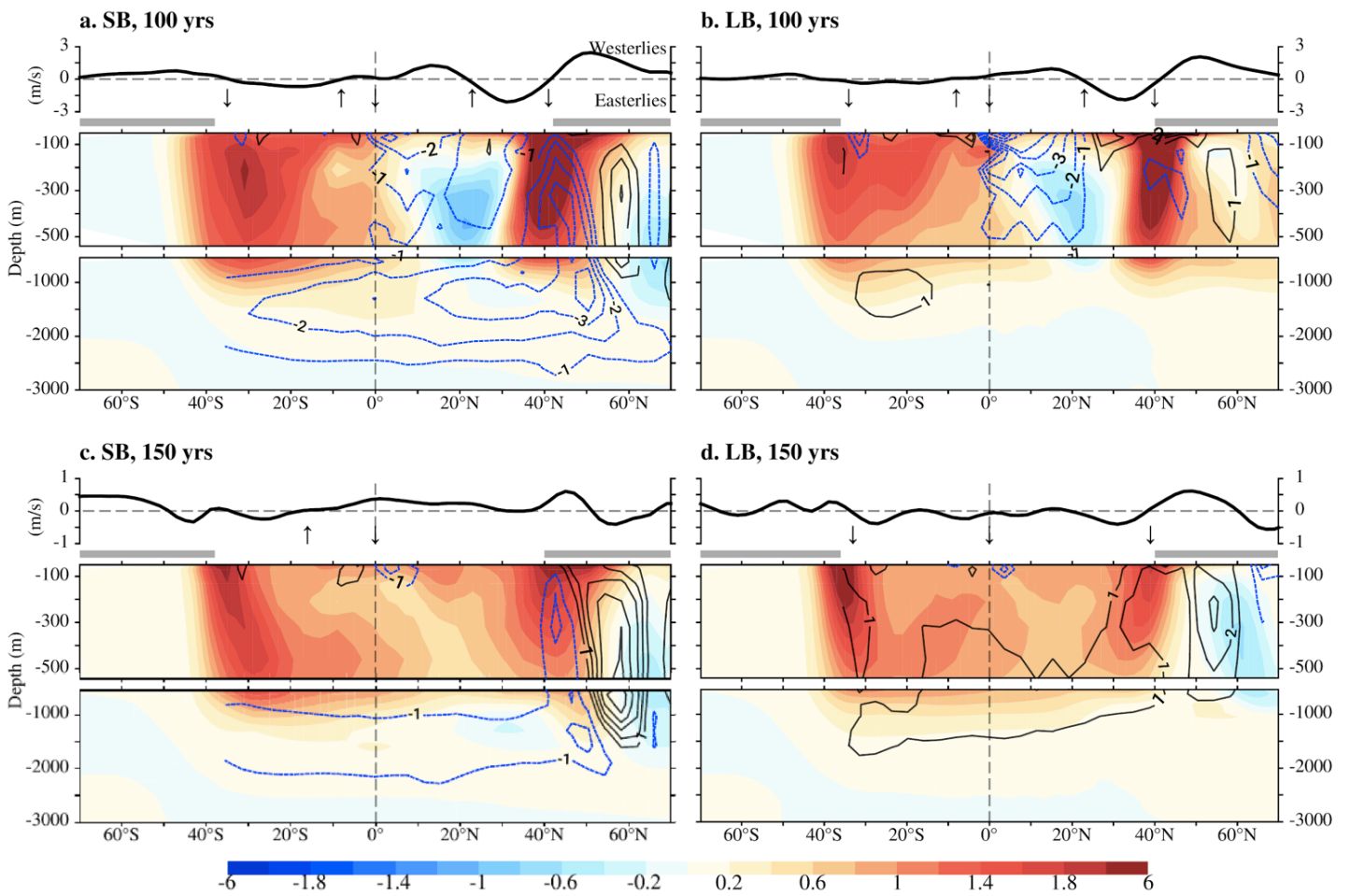


Fig. 5. Anomalies (relative to the cold state; shown in Supp. Fig. 1) in the zonally averaged zonal wind (in m/s; first panel from the top), and in the ocean temperature (in °C; shading) and overturning streamfunction (in $\text{Sv} = 10^6 \text{ m}^3/\text{s}$; contours, with clockwise/anticlockwise circulation in solid, black/dashed, blue line, and only north of 35°S) above and below 540 m (second and third panels respectively) in the small (**a,c**) and large (**b,d**) basin in year 100 (**a,b**) and 150 (**c,d**). Up/down arrows (first panels in **a–d**) reflect anomalous wind-driven upwelling/downwelling in ice-free regions. Sea ice extent—concentration above 15 %—is also shown in gray between the first and second panels in each basin and year. The shading color scale of the ocean temperature is adapted for a better view of the values in the range ± 2 °C.

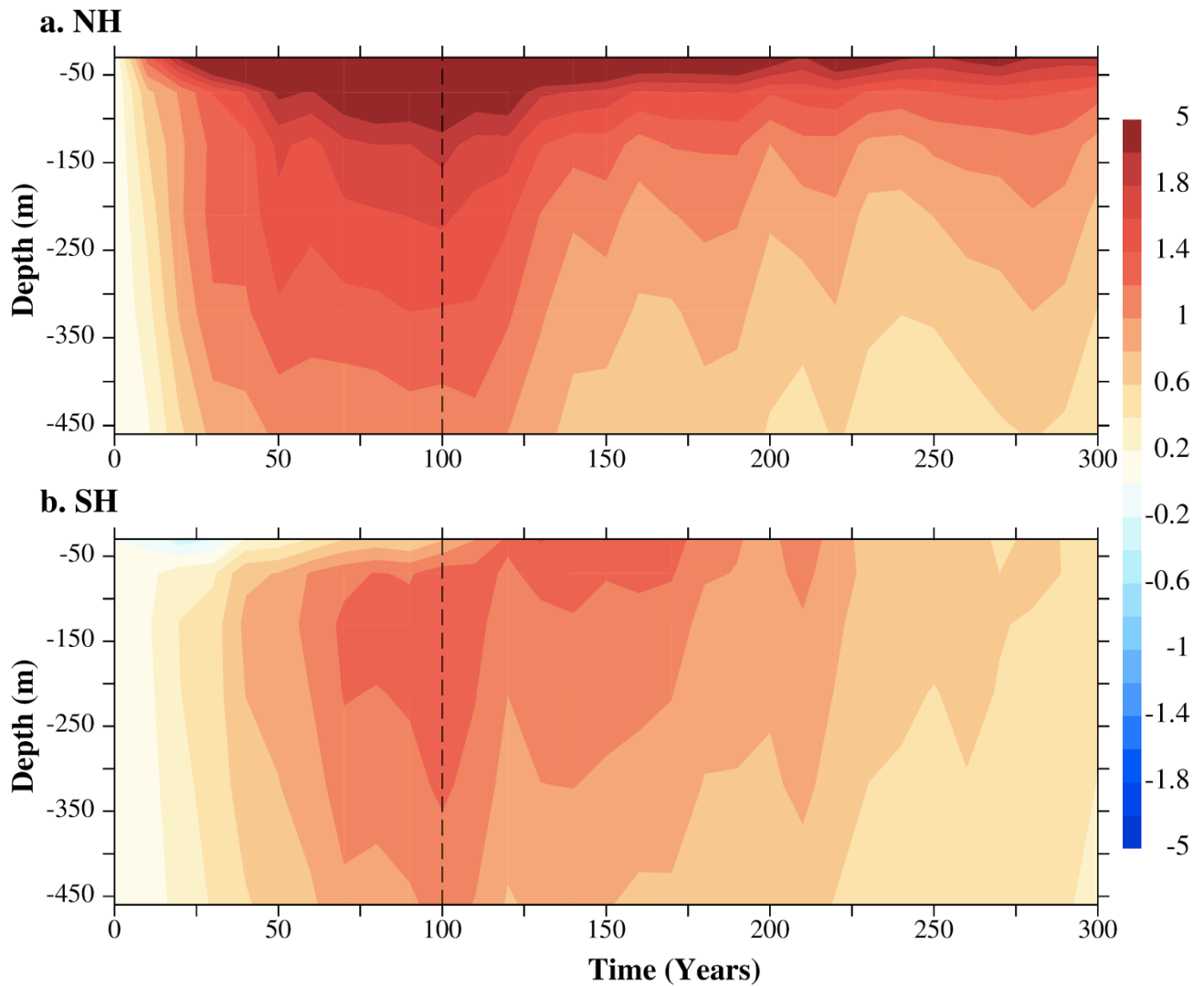


Fig. 6. Hovmöller plot of the zonally averaged ocean temperature anomalies (in $^{\circ}\text{C}$; with respect to the cold state) between the surface and 460 m at **(a)** NH mid-latitude (40°N – 60°N) and **(b)** SH (30°S – 50°S) both between 95°W and 5°E ; respectively orange and purple areas in Fig. 2a). The shading color scale of the ocean temperature is adapted for a better view of the values in the range $\pm 2^{\circ}\text{C}$. The vertical dashed line marks the year 100, when the forcing is switched off.

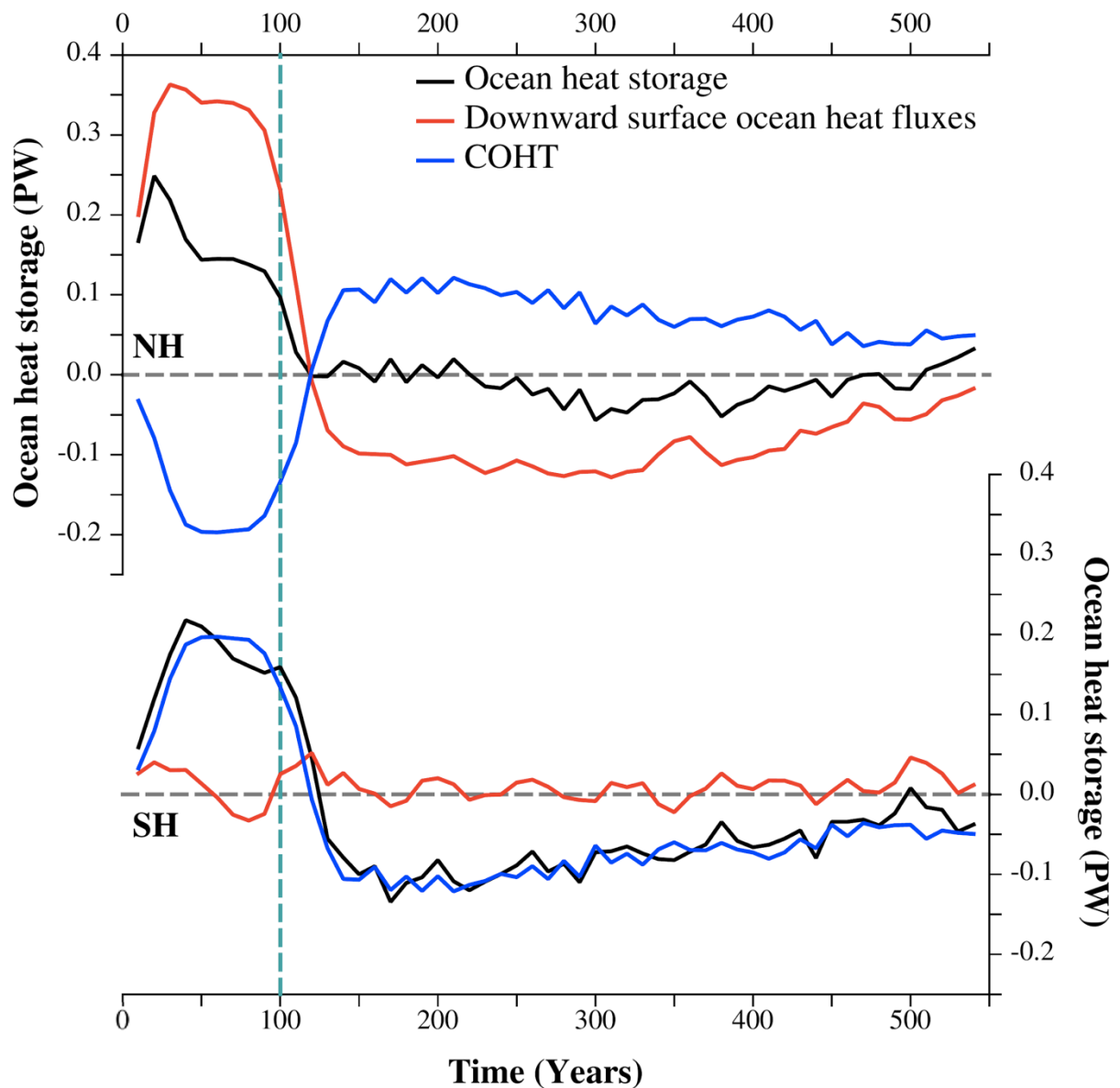


Fig. 7. Change in ocean heat storage (in PW; black line) in the NH and SH (top and bottom panel respectively), calculated as the difference between the two main contributions: the total horizontally integrated downward surface heat flux (in PW; red line), and the COHT (in PW; blue line; with positive values for a northward/southward COHT in the NH/SH and vice versa). The heat stored in the cryosphere (e.g., as melting snow and sea ice) is found comparatively much smaller and hence not shown. Time series are smoothed with a 3-point running mean. The vertical dashed line marks the year 100, when the forcing is switched off.

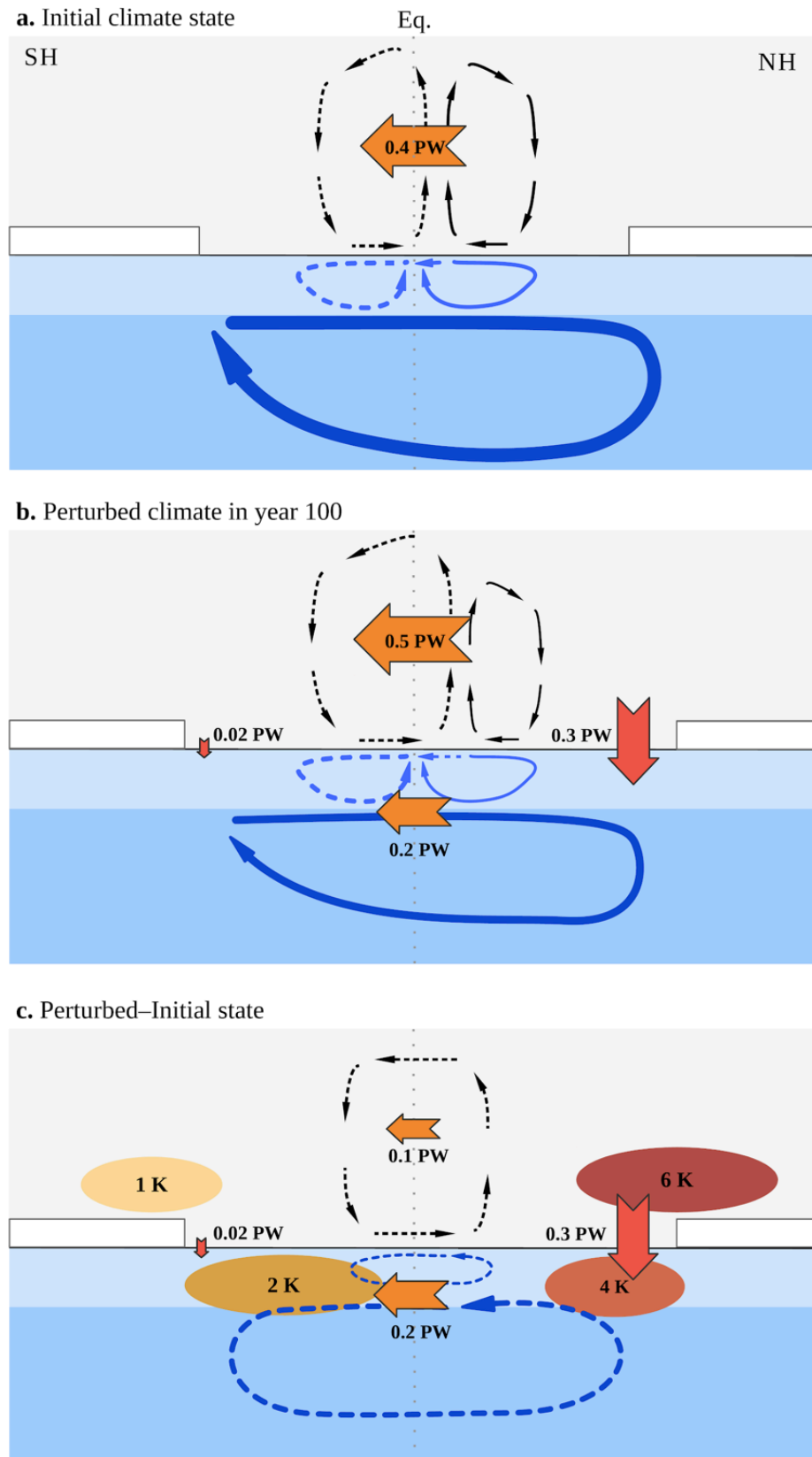


Fig. 8. Atmospheric and upper and deep oceanic circulations (black, light blue, and dark blue arrows, respectively), as well as the hemispheric mean air–sea heat flux, and the cross-equatorial heat transports (red and orange arrows, respectively) in **(a)** the cold state and **(b)** perturbed climate. **(c)** Changes in such magnitudes between both climate states, together with a rough estimate of the warming anomalies in high-latitude SATs and mid-latitude SSTs in both hemispheres. Hemispheric mean surface fluxes in the cold state **(a)** show negligible values compared to other contributions and are therefore not shown. Note the magnitude of the surface flux and heat transport changes will vary with the strength of the forcing applied; here it is shown for the simulations with global forcing (Section 2).



Paleoceanography and Paleoclimatology

Supporting Information for

**Polar phasing and cross-equatorial heat transfer following a simulated abrupt NH
warming of a glacial climate**

E. Moreno-Chamarro ^{1,2,*}, D. Ferreira ³, and J. Marshall ¹

1. Department of Earth, Atmospheric, and Planetary Sciences. Massachusetts Institute of Technology, Cambridge, MA, USA.

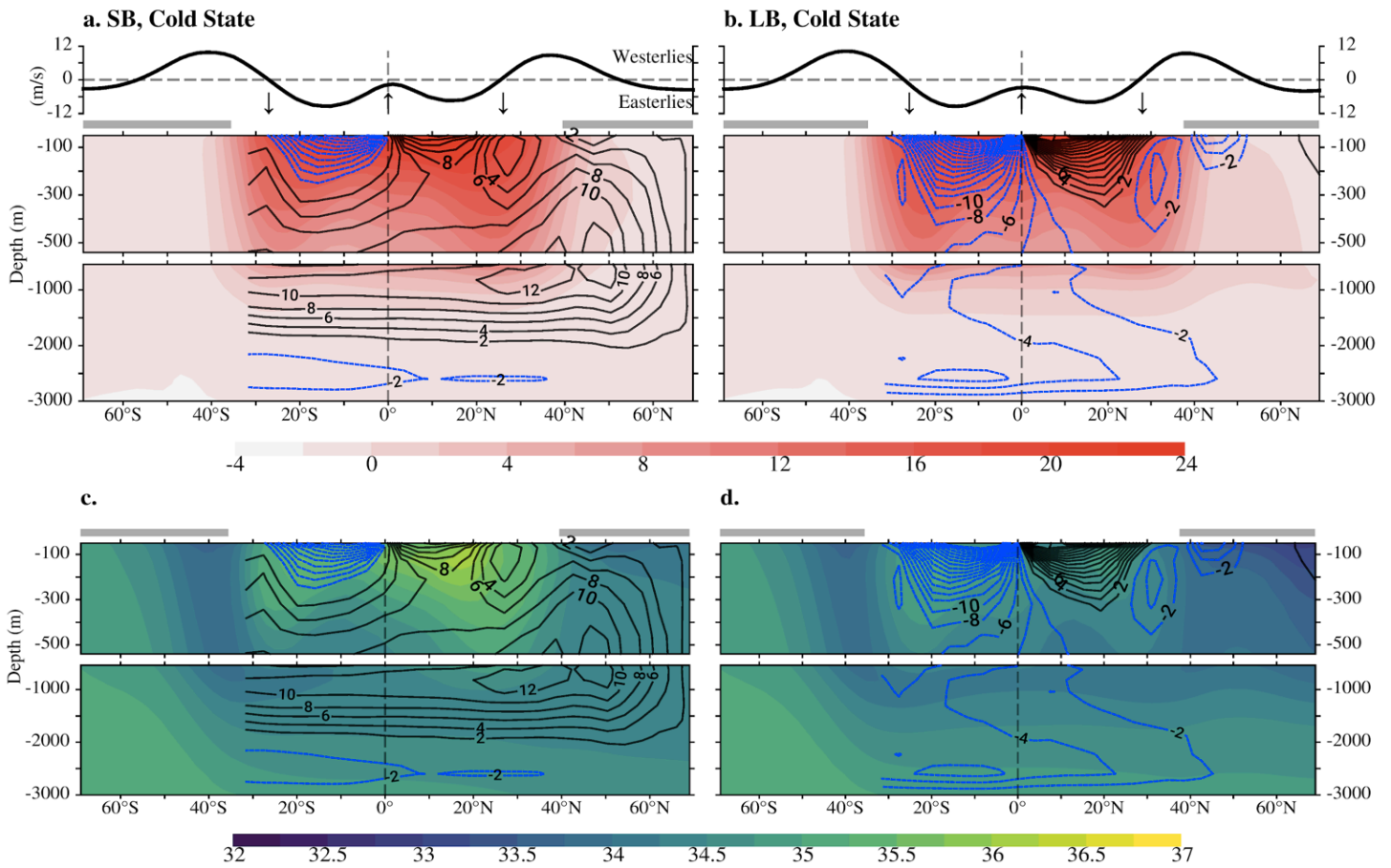
2. Present address: Barcelona Supercomputing Center (BSC), Barcelona, Spain.

3. Department of Meteorology, University of Reading, Reading, UK

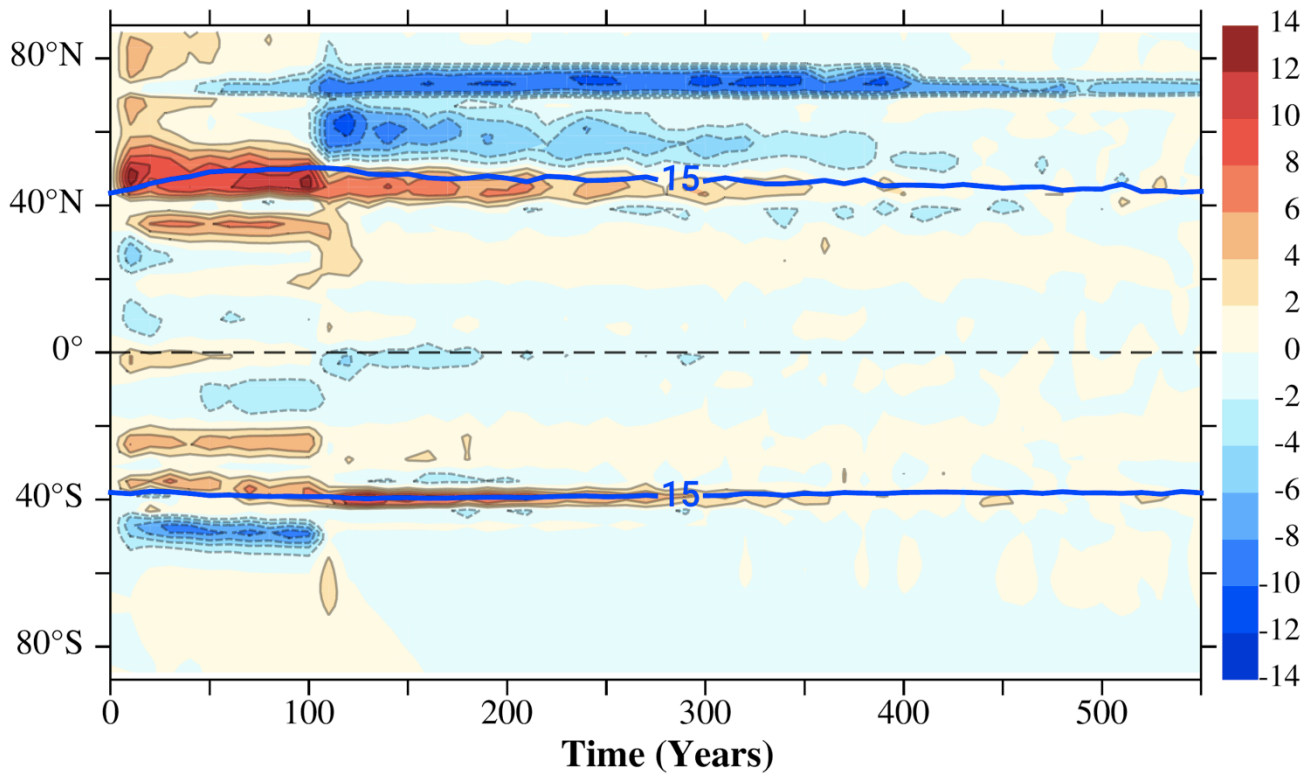
* Corresponding author: eduardo.moreno@bsc.es

Contents of this file

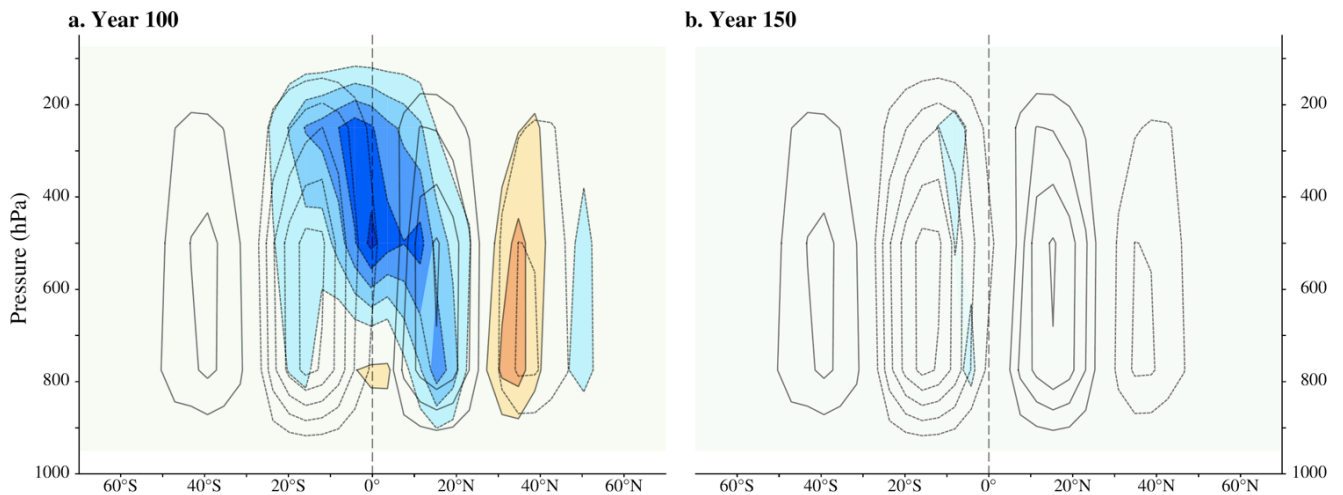
Supporting Figures (Supp. Figs) 1 to 10.



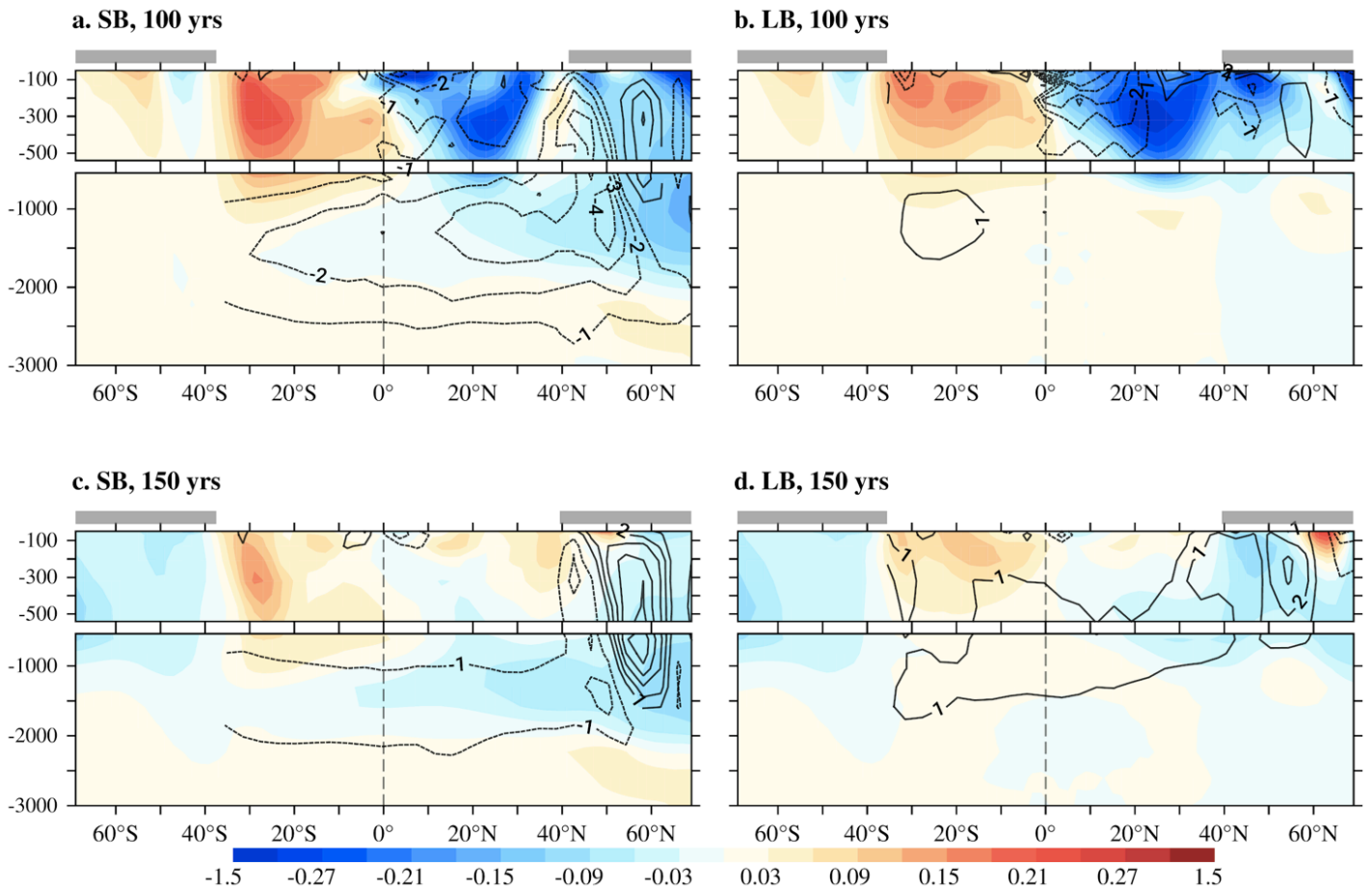
Supp. Fig. 1. (a,b). Zonally-averaged zonal wind (top panel; in m/s), and ocean temperature (shading, in °C) and overturning circulation (in $\text{Sv} = 10^6 \text{ m}^3/\text{s}$; contours, with clockwise/anticlockwise circulation in solid, black/dashed, blue line, and only north of 35°S) above and below 540 m (second and third panels respectively) in **(a)** the small and **(b)** large basins in the cold state. Up/down arrows (top panels) reflect anomalous wind-driven upwelling/downwelling in ice-free regions. Sea ice extent—concentration above 15 %—is also shown in gray between the top and middle panels in each basin and year. **(c,d).** As in **(a,b)** but for the ocean salinity (in psu).



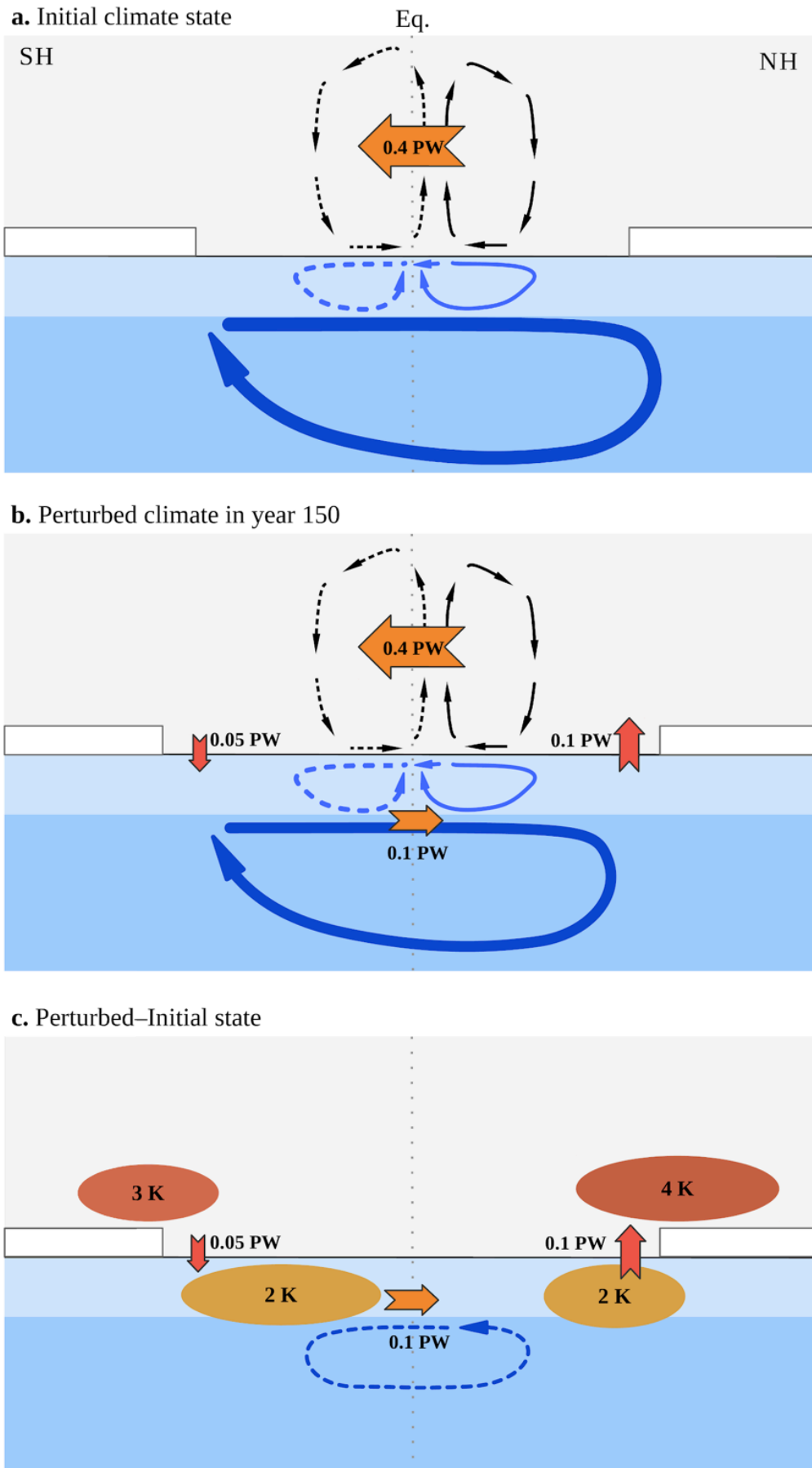
Supp. Fig. 2. Zonally averaged air–sea heat flux anomalies (positive downward, in W/m^2 ; relative to the cold state). Also shown in each basin is the sea ice extent limit, as the 15% sea ice concentration (blue contours).



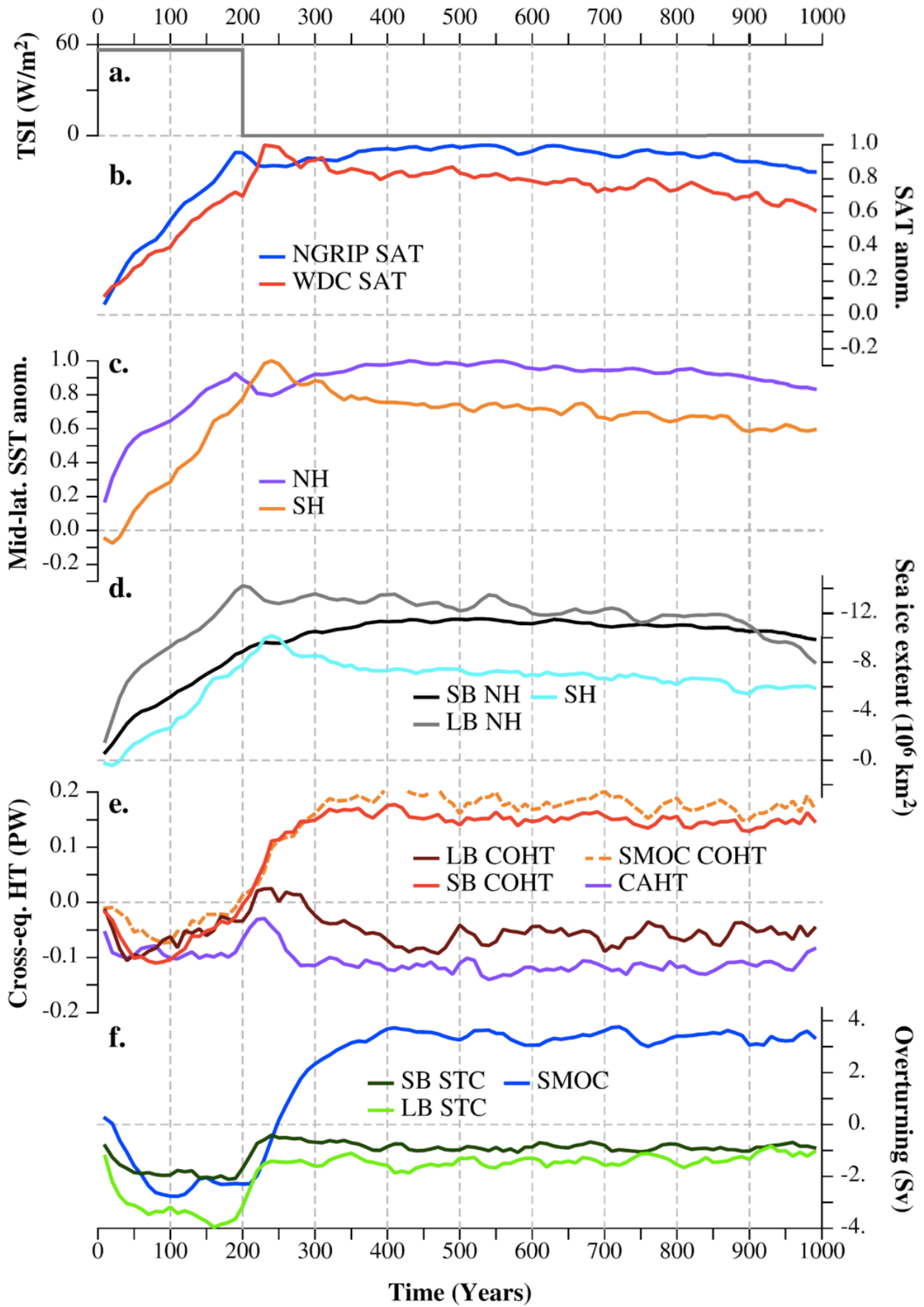
Supp. Fig. 3. Anomalies (relative to the cold state) in the zonally averaged mass streamfunction (color shading every 5 kg/s , the zero contour is omitted) in year (a) 100 and (b) 150. Climatology in the cold state is in black contours (every 20 kg/s).



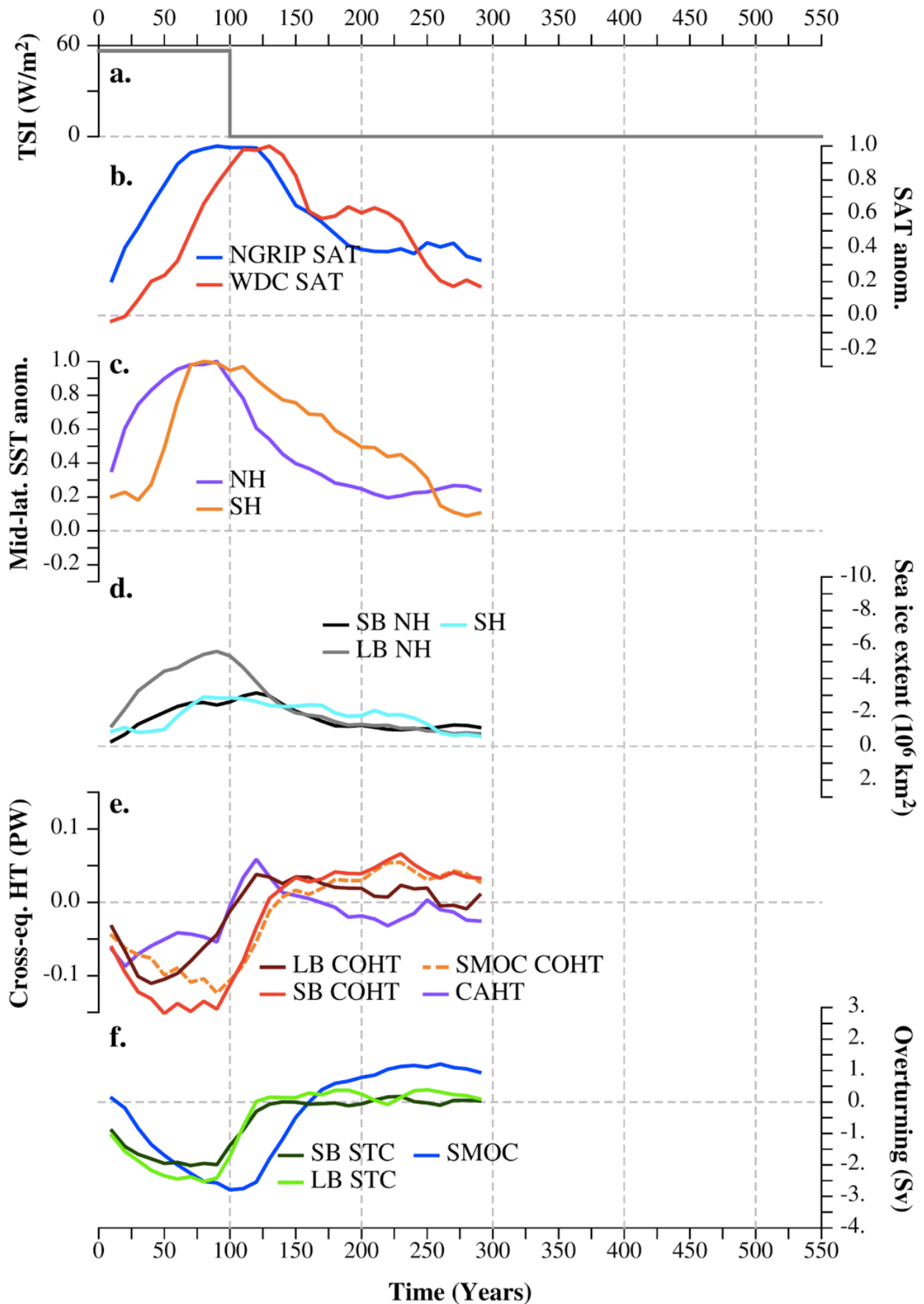
Supp. Fig. 4. Anomalies (relative to the cold state, shown in Supp. Fig. 1c,d) in the zonally averaged ocean salinity (shading; in psu) and overturning streamfunction (contours; in Sv; with clockwise/anticlockwise circulation in solid/dashed line; only north of 35°S) above and below 540 m (top and bottom panels respectively) in the small (left) and large basin (right) in year **(a, b)** 100 and **(c, d)** 150. The shading color scale is adapted for a better view of the salinity values in the range ± 0.5 psu. Sea ice extent—concentration above 15%—is indicated by the gray shading on top of the top panel in each basin.



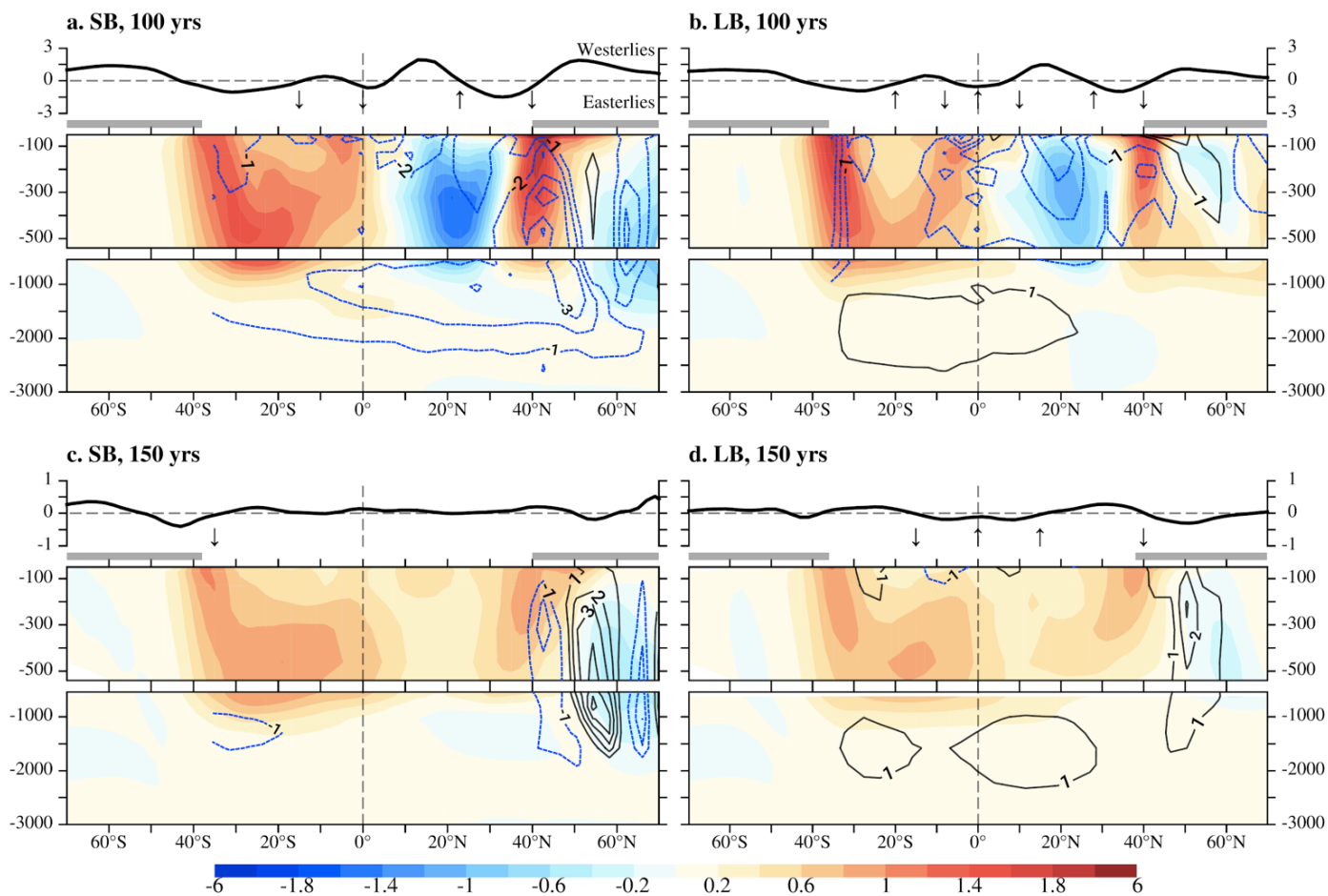
Supp. Fig. 5. As in Fig. 8, but between the cold state and the climate in year 150.



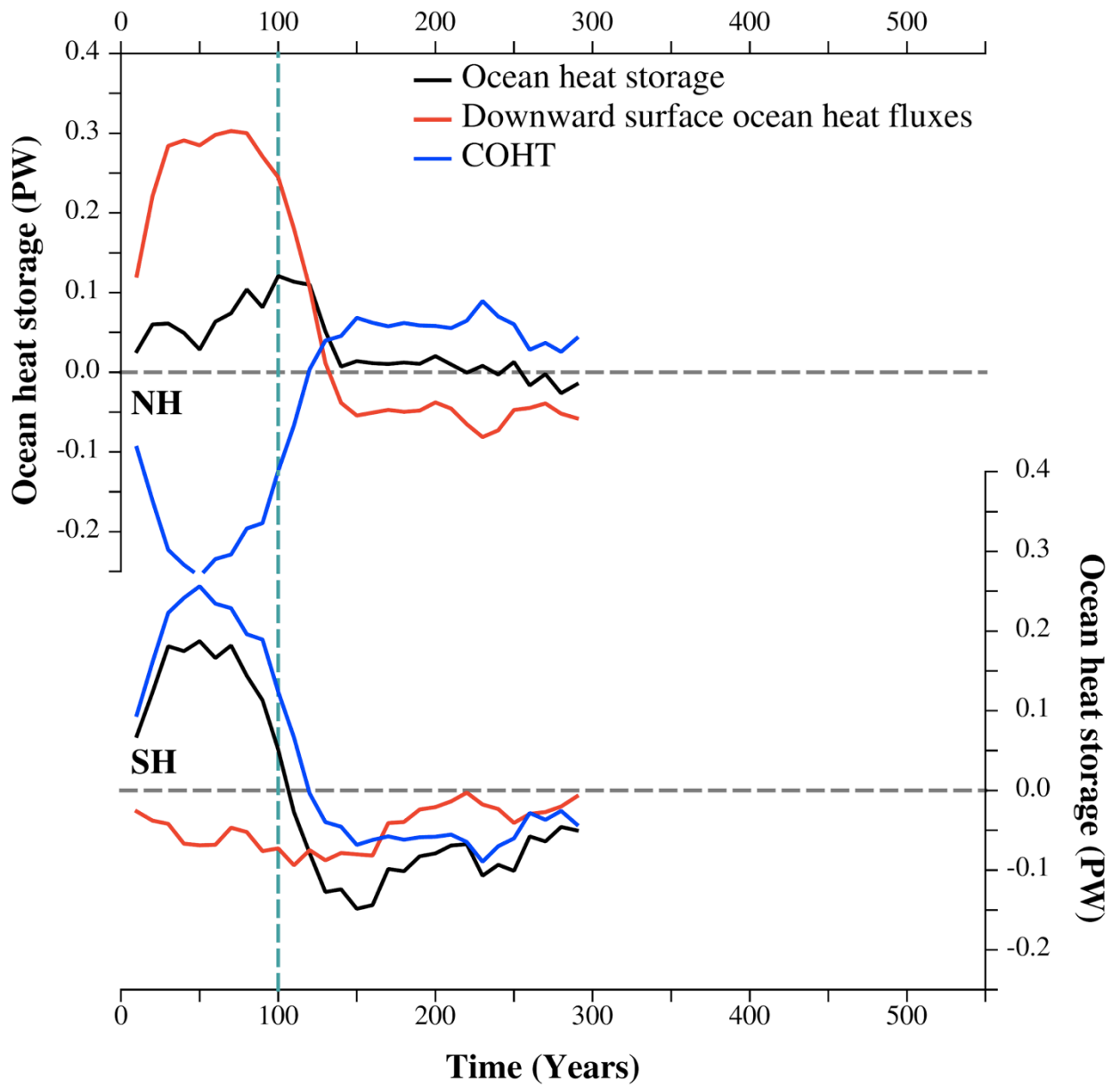
Supp. Fig. 6. As in Fig. 3, but in the experiment with a 200-year forcing. Maximum anomaly values are about 16 °C and 4 °C for the SATs (b) and 7 °C and 3 °C for the SSTs (c) in the NH and SH respectively.



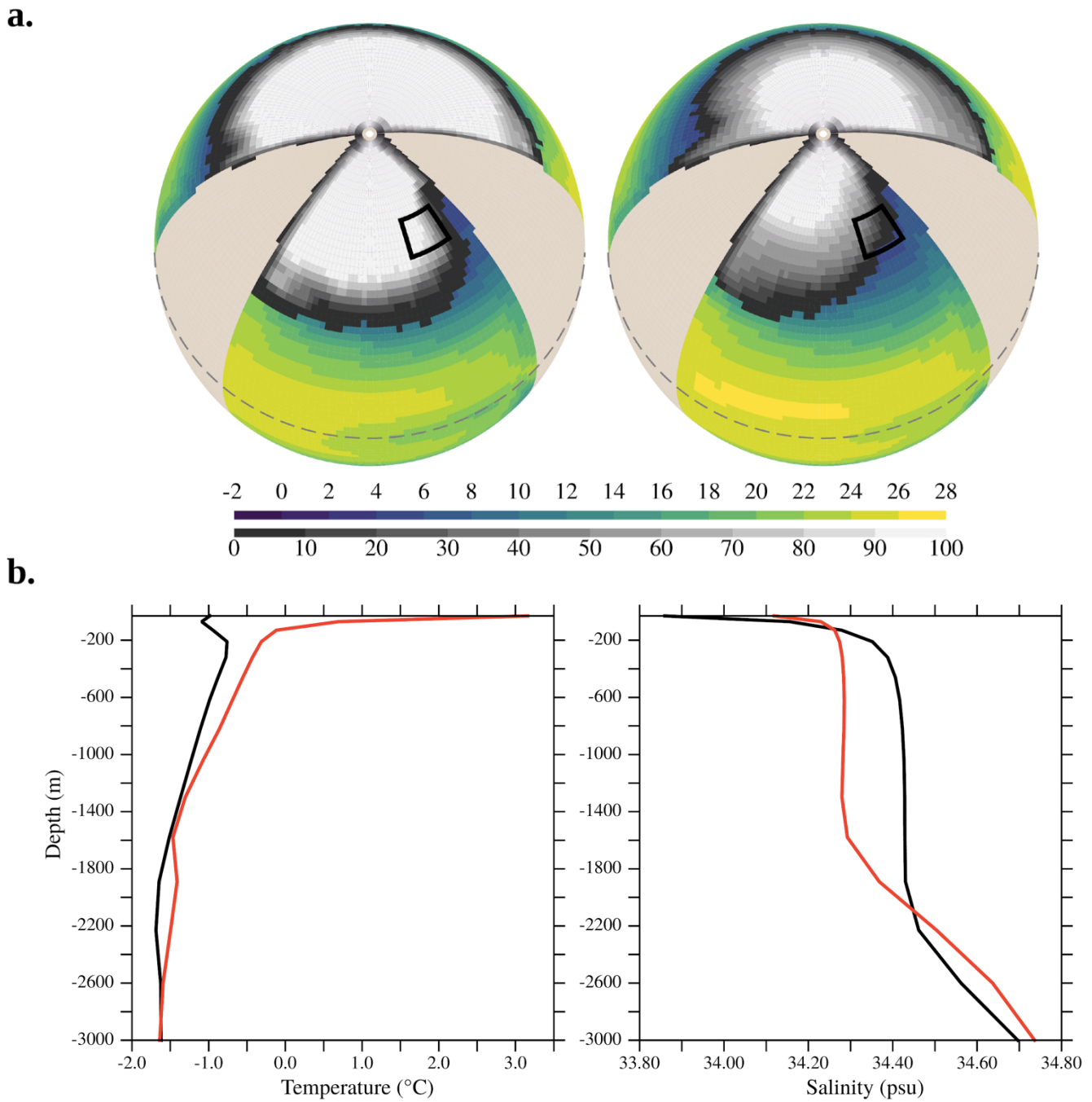
Supp. Fig. 7. As in Fig. 3, but in the experiment with forcing only in the NH. Maximum anomaly values are about 4 °C and 2 °C for the SATs (b) and 3 °C and 1 °C for the SSTs (c) in the NH and SH respectively.



Supp. Fig. 8. As in Fig. 5, but in the experiment with forcing only in the NH. Note that the color scale of the ocean temperature is the same as in Fig. 5 for comparison.



Supp. Fig. 9. As in Fig. 7, but in the experiment with forcing only in the NH.



Supp. Fig. 10. a) As in Fig. 2, but for SST (in °C; dark blue-yellow shading) and sea ice concentration (in %; gray shading) in the cold state (left) and in year 100 (right). Black box outlines the area between 10°W–30°W and 55°N–65°N where the **(b)** vertical profiles of ocean temperature (in °C; left) and salinity (in psu; right) are calculated in the cold state (black line) and in year 100 (red).